Research Square

Preprints are preliminary reports that have not undergone peer review.
They should not be considered conclusive, used to inform clinical practice,
or referenced by the media as validated information.

PI3Kγ-dependent macrophage reprogramming overcomes microenvironmental tumor protection in sunitinib-challenged renal cancer

Zhangxin He

jfhzx@163.com

The Fourth Affiliated Hospital of Soochow University https://orcid.org/0009-0001-4459-1995

Xiaorui Hou

The Fourth Affiliated Hospital of Soochow University

Xin Ye

The First Affiliated Hospital of Soochow University

Anguo Zhao

The Fourth Affiliated Hospital of Soochow University

Xin Chen

The Fourth Affiliated Hospital of Soochow University

Yufeng Hou

The Fourth Affiliated Hospital of Soochow University

Jingang Jian

The Fourth Affiliated Hospital of Soochow University

Xuedong Wei

The First Affiliated Hospital of Soochow University

He Wang

The First Affiliated Hospital of Soochow University

Hao Jiang

The First Affiliated Hospital of Soochow University

yuhua Huang

https://orcid.org/0000-0002-0341-0078

Di Jiao

The Fourth Affiliated Hospital of Soochow University

Hongbo Xu

The Fourth Affiliated Hospital of Soochow University

Jianquan Hou

The Fourth Affiliated Hospital of Soochow University

Article

Keywords:

Posted Date: November 13th, 2026

DOI: https://doi.org/10.21203/rs.3.rs-11707079/v1

License: This work is licensed under a Creative Commons Attribution 4.0 International License.
Read Full License

Additional Declarations: There is **NO** Competing Interest.

Title

PI3Kγ-dependent macrophage reprogramming overcomes microenvironmental tumor protection in sunitinib-challenged renal cancer

Authors

Zhangxin He, [1]* Xiaorui Hou, [1]* Xin Ye, [2]* Anguo Zhao, [1] Xin Chen, [1] Yufeng Hou, [1] Jingang Jian, [1] Xuedong Wei, [2] He Wang, [2] Hao Jiang, [2] Yuhua Huang, [2]† Di Jiao, [1]† Hongbo Xu, [1]† Jianquan Hou[1]†

Affiliations

1. Department of Urology, The Fourth Affiliated Hospital of Soochow University (Suzhou Dushu Lake Hospital), Suzhou, Jiangsu 215000, China.
2. Department of Urology, The First Affiliated Hospital of Soochow University, Suzhou, Jiangsu 215006, China.

*These authors contributed equally to this work.

†Corresponding authors.

Email: sdfyy_hyh@163.com; djiao@suda.edu.cn; xhbcs1123@163.com; houjianquan@suda.edu.cn

Abstract

In sunitinib-treated renal cancer, tumor-associated macrophages (TAMs) can support tumor survival while suppressing antitumor immunity, but whether both effects can be reversed simultaneously is unclear. We identify phosphoinositide 3-kinase γ (PI3Kγ) as a macrophage-associated target and develop a protease-responsive, macrophage-directed nanocarrier (IMNMP) delivering the PI3Kγ inhibitor eganelisib (IPI-549). Sunitinib-conditioned renal cancer cells induced a tumor-supportive macrophage state with increased PI3Kγ and enhanced tumor cell protection. Genetic PI3Kγ silencing or IMNMP attenuated this protection, promoted macrophage costimulatory/inflammatory programs and enhanced $CD8^+$ T-cell responses. In vivo, IMNMP plus sunitinib improved tumor control and produced an immunostimulatory microenvironment with increased macrophage costimulation and $CD8^+$ T-cell infiltration. Bulk and single-cell transcriptomics linked treatment to antigen-presentation, interferon-response and effector immune programs in tumor-associated myeloid cells. Together, PI3Kγ-dependent macrophage function is an actionable component of sunitinib-treated renal cancer, and macrophage-directed PI3Kγ inhibition may simultaneously reduce microenvironmental tumor protection and strengthen antitumor immunity.

INTRODUCTION

Combining immune checkpoint therapy with inhibitors of vascular endothelial growth factor signaling has reshaped systemic treatment of renal cell carcinoma (RCC). Long-term follow-up of pembrolizumab-axitinib, lenvatinib-pembrolizumab and nivolumab-cabozantinib has demonstrated durable clinical benefit over sunitinib *(1-3)*. Sustained responses to nivolumab-ipilimumab and biomarker analyses of kinase-inhibitor-containing combinations further underscore the importance of the immune microenvironment in treatment response *(4, 5)*. These observations indicate that therapeutic efficacy in RCC is determined not only by direct effects on malignant cells but also by the functional state and organization of tumor-infiltrating immune populations.

Tumor-associated macrophages (TAMs) are a prominent component of the RCC immune microenvironment. Single-cell and spatial studies have identified recurrence-associated macrophage states, macrophage populations that coexist with exhausted T cells, and marked intratumoral heterogeneity in macrophage organization and function *(6-8)*. Tissue-resolved and multimodal analyses further link these populations to intratumoral location, antigen-presentation-associated architecture and treatment-induced reprogramming *(9-12)*. Immune-network organization and chemokine-defined macrophage–T-cell neighborhoods have also been associated with checkpoint sensitivity *(13, 14)*. Specific APOE-, SPP1- and MARCO-associated macrophage programs have been linked to immune suppression and $CD8^+$ T-cell dysfunction *(15-17)*. Together, these findings suggest that macrophages may influence both tumor cell fitness and local immune competence during therapy. Whether macrophage-directed intervention can simultaneously reduce tumor-protective support and restore antitumor immune activity under sunitinib treatment pressure remains unclear.

PI3Kγ provides a tractable molecular entry point for macrophage-directed intervention. Myeloid PI3Kγ sustains immunosuppressive transcriptional programs, and its inhibition enhances antitumor T-cell responses and the activity of immune checkpoint therapy in experimental models *(18, 19)*. Eganelisib (IPI-549), a selective PI3Kγ inhibitor developed for immuno-oncology, has been evaluated clinically both as monotherapy and in combination with checkpoint blockade *(20-22)*. Paired biopsy analyses from eganelisib-containing regimens have further associated PI3Kγ inhibition with macrophage reprogramming and immune activation. However, whether PI3Kγ-dependent macrophage functions contribute to tumor protection under sustained kinase-inhibitor pressure, and whether this compartment can be selectively targeted to improve therapy, remain incompletely defined.

Selective modulation of tumor-associated macrophages requires both access to the tumor microenvironment and preferential exposure of the intended myeloid compartment *(23)*. The M2 macrophage-targeting peptide (M2pep) provides a sequence-dependent recognition motif for selected murine macrophage populations and has been incorporated into nucleic-acid carriers and exosome-based systems for TAM-directed delivery *(24-27)*. Related macrophage-directed formulations have been evaluated in RCC and in strategies targeting M2-like populations *(28, 29)*. In parallel, protease-cleavable polyethylene glycol (PEG) architectures can modulate particle shielding, structural organization, and cargo availability within protease-rich tumor environments *(28-32)*. We therefore integrated a long matrix metalloproteinase-9 (MMP-9)-cleavable PEG component with a shorter M2pep-bearing PEG component to construct IMNMP, a nanocarrier that couples IPI-549 delivery with MMP-9 responsiveness and macrophage-associated uptake.

Here, we examined whether PI3Kγ-associated macrophage function contributes to tumor protection during sunitinib treatment and whether macrophage-directed PI3Kγ inhibition can simultaneously enhance local antitumor immunity. Using macrophage-conditioning models, genetic and pharmacological PI3Kγ perturbation, renal tumor models, and complementary bulk and single-cell transcriptomics, we show that prolonged exposure to sunitinib-conditioned tumor cells promotes a tumor-supportive macrophage state associated with increased PI3Kγ expression. PI3Kγ-directed macrophage modulation reduces macrophage-mediated tumor protection, promotes immunostimulatory myeloid programs, and improves the response to sunitinib. These findings identify PI3Kγ-associated macrophage function as a therapeutically actionable component of the renal cancer microenvironment under targeted-therapy pressure (Scheme 1).

RESULTS

PIK3CG expression is associated with macrophage populations in renal cancer

Analysis of public RCC datasets revealed elevated *PIK3CG* expression in renal tumors relative to normal kidney tissues and variable correlations with macrophage-associated transcriptional features. In the initial comparison of 538 renal tumors and 72 normal kidney samples, tumor tissues showed higher PIK3CG expression (Fig. 1A–C). Across six RCC cohorts, Spearman correlations between *PIK3CG* expression and macrophage-associated transcriptional signatures ranged from 0.09 to 0.86, with four cohorts showing coefficients of 0.70 or higher (Fig. 1B). Positive correlation estimates with CD163 across all six cohorts further highlighted a recurring association with CD163-associated macrophage features, ranging from 0.26 to 0.72 (Fig. 1C). Single-cell RNA sequencing further showed that *PIK3CG* expression was more prominent in immune cell populations, including macrophages, than in annotated tumor cells (Fig. 1D–G). In the bulk tumor analysis, PIK3CG correlated with both the macrophage signature score ($r = 0.592$, $P = 4.99 \times 10^{-52}$) and CD163 expression ($r = 0.679$, $P = 7.69 \times 10^{-74}$; Fig. 1H, I). These associations provided a rationale to investigate whether PI3Kγ influences macrophage function in RCC.

Multiplex immunofluorescence of paired renal tumor and peritumoral tissues quantified $CD68^+$ and $CD68^+CD163^+$ cell populations and PI3Kγ positivity within the latter population (Fig. 1J–P). The detection of PI3Kγ in $CD68^+CD163^+$ cells complemented the transcriptomic findings by providing protein-level evidence of its expression in $CD163^+$ macrophages. Together, these observations supported further functional investigation of macrophage PI3Kγ in the context of renal cancer treatment. We next examined how prolonged coculture with sunitinib-exposed renal cancer cells affected macrophage function and whether PI3Kγ inhibition could modulate the resulting changes.

Prolonged tumor conditioning establishes macrophage-mediated protection during sunitinib exposure

Repeated sunitinib exposure generated a sunitinib-stressed Renca cell population (Renca-s; Fig. 2A). The half-maximal inhibitory concentration (IC_{50}) of sunitinib increased from 3.35 μM in parental Renca cells to 6.304 μM in Renca-s cells, representing a 1.88-fold increase (Fig. 2B). Compared with the parental cells, Renca-s cells exhibited a significantly lower apoptosis rate following sunitinib treatment, the representative apoptosis rates for the parental cells and Renca-s cells were 52.0% and 20.9%, respectively. The apoptosis rate in Renca-s cells decreased by 31.1 percentage points, suggesting that Renca-s cells are resistant to sunitinib, ($P = 0.0084$; Fig. 2C, D; fig. S1). Given the consistency between the dose-response relationship and the apoptosis assay results, Renca-s is defined as a drug-treated tumor population for studying macrophage-mediated regulation.

We next conditioned RAW264.7 macrophages through noncontact coculture with parental Renca or Renca-s cells for 12 h or 7 days (Fig. 2E). In representative flow cytometry plots, the CD206-positive fraction increased from 0.8% to 15.4% after parental Renca conditioning and from 2.3% to 20.2% after Renca-s conditioning when exposure was extended from 12 h to 7 days (Fig. 2F, G). After 7 days of coculture, supernatant concentrations of MMP-9, interleukin-10 (IL-10), and transforming growth factor-β (TGF-β) were higher in the Renca-s conditioning group than in the parental Renca conditioning group ($P < 0.0001$, $P = 0.0477$, and $P < 0.0001$, respectively; Fig. 2H–J). We designated macrophages conditioned for 7 days with parental Renca cells as TAM-trend macrophages and those conditioned with Renca-s cells as TAM-like macrophages (Fig. 2P). The increased CD206-positive fraction and immunoregulatory secretory output defined the TAM-like state and prompted a direct test of its ability to protect tumor cells.

During sunitinib treatment, coculture with TAM-like macrophages retained 1.29 fold the viability of cells cocultured with unconditioned macrophages ($P < 0.0001$; Fig. 2K, L). Compared with unconditioned macrophages, TAM-like macrophages exhibited higher arginase 1 (Arg1) and Mrc1 transcript levels, lower Nos2 transcript levels (Fig. 2M–O), linking tumor protection to an M2-like transcriptional program. PI3Kγ protein abundance, normalized to GAPDH, was 6.64 times that in unconditioned macrophages ($P = 0.0134$; Fig. 2Q, R). Prolonged conditioning therefore coupled an immunoregulatory macrophage phenotype to tumor protection and increased PI3Kγ abundance, identifying a functional state to target through macrophage-directed inhibitor delivery.

IMNMP exhibits MMP-9 responsiveness and enhanced macrophage uptake

IMNMP was formulated with the PI3Kγ inhibitor IPI-549, the MMP-9–responsive lipid conjugate DSPE–GPLGVRG–$mPEG_{10K}$, and the M2pep-functionalized lipid conjugate DSPE–$mPEG_{500}$–M2pep (Fig. 3A). Supplier-provided synthesis records and proton nuclear magnetic resonance (^1H NMR) were consistent with the expected structures of both polymer conjugates (Fig. S2, S3). Formulations with different component ratios exhibited distinct hydrodynamic diameters and polydispersity indices, guiding formulation selection based on particle size and dispersity (Fig. 3B). The selected formulation exhibited a hydrodynamic diameter of 211.9 nm and a polydispersity index (PDI) of 0.113 in a representative dynamic light scattering (DLS) measurement (Fig. 3C). The selected formulation also showed an encapsulation efficiency (EE) of 84.2% and a drug loading (DL) of 2.8% for IPI-549, indicating efficient retention of the drug within the nanoparticles at a defined drug-to-carrier ratio. Additional characterization assessed the zeta potential and monitored changes in hydrodynamic diameter and PDI during storage (Fig. S4). IMNMP exhibited a weakly negative zeta potential, which typically helps reduce nonspecific adsorption and particle aggregation and thus contributes to colloidal dispersion stability. After 18 days of storage, neither the hydrodynamic diameter nor the PDI of IMNMP changed significantly, suggesting that the formulation exhibits good storage stability over the test period and provides a stable formulation basis for subsequent in vitro and in vivo evaluations.

Treatment with 20 nM MMP-9 altered the chromatographic profile of IMNMP, reducing the signal at a retention time of approximately 14–15 min, and decreased its representative hydrodynamic diameter from 211.9 to 127.4 nm (Fig. 3D, E, H). These changes supported MMP-9–responsive remodeling of IMNMP, consistent with the PEG-layer remodeling illustrated in the formulation design. We next examined MMP-9 abundance in paired human renal tumor and peritumoral tissues. After normalization to tissue mass, MMP-9 levels were approximately fivefold higher in tumors than in matched peritumoral tissues ($P = 0.0407$; Fig. 3F). This tumor-associated enrichment provided a tissue-level rationale for using MMP-9 as an environmental trigger for carrier remodeling. After 72 h, cumulative IPI-549 release reached approximately 42% under the high–MMP-9 condition and 32% under the low–MMP-9 condition (Fig. 3G). The greater cumulative release under high–MMP-9 conditions connected the structural response to enhanced drug release, supporting an enzyme-responsive delivery strategy.

IMNMP enhances macrophage-associated fluorescence and promotes an immunostimulatory phenotype

To evaluate the contributions of M2pep functionalization and MMP-9 responsiveness, we compared IMNMP with three control formulations: INP, lacking both functional elements; IMNP, retaining M2pep but lacking the MMP-9–responsive component; and INMP, retaining the MMP-9–responsive component but lacking M2pep (Fig. 4A). Among the tested

formulations, fluorescently labeled IMNMP exhibited the highest early macrophage-associated fluorescence signal (Fig. 4B, C). To test whether this advantage depended on MMP-9 responsiveness, an additional IMNMP group was evaluated in the presence of the matrix metalloproteinase (MMP) inhibitor Galardin. Representative histograms of the IMNMP-plus-Galardin group showed a rightward shift in the fluorescein isothiocyanate (FITC) fluorescence peak relative to INP at both 0.5 and 2 h (Fig. 4B), consistent with a retained M2pep-associated contribution to macrophage fluorescence when MMP-9 responsiveness was inhibited. To assess cell-associated fluorescence in a mixed-cell system, cyanine 5 (Cy5)-prelabeled TAM-like macrophages were cocultured with unlabeled Renca-s cells at a 1:1 ratio and exposed to FITC-labeled INP or IMNMP. Flow cytometry distinguished the two cell populations, and representative histograms showed differences in FITC fluorescence distributions between the formulations at 0.5 and 2 h (Fig. S5). Collectively, these results support that both M2pep functionalization and MMP-9 responsiveness contribute to enhanced early macrophage-associated fluorescence and that the mixed-cell system enables population-resolved detection under identical exposure conditions.

IMNMP treatment increased the proportion of $CD86^+$ cells among $F4/80^+$ RAW264.7-derived TAM-like macrophages compared with INP treatment. Representative flow cytometry plots showed CD86 positivity of 57.0% after INP treatment and 88.6% after IMNMP treatment, consistent with the difference observed across independent preparations ($P < 0.0001$; Fig. 4D, E). To examine this response in primary macrophages, bone marrow-derived macrophages (BMDMs) were differentiated in macrophage colony-stimulating factor-containing medium and subsequently conditioned through noncontact Transwell coculture with Renca-s cells for 7 days (Fig. S6). IMNMP treatment also increased the proportion of $CD86^+$ cells among $CD45^+CD11b^+$ BMDMs compared with INP treatment ($P = 0.0074$; Fig. 4F, G). The consistent increase in $CD86^+$ cells across RAW264.7-derived TAM-like macrophages and BMDMs suggests that IMNMP promotes an M1-associated phenotypic shift in both cell line-derived and primary macrophage models.

Compared with INP, IMNMP treatment increased *Tnf*, *Cxcl9*, and *Nos2* transcript levels while reducing *Mrc1* and *Arg1* expression. *Cxcl10* expression was also numerically higher, although the difference between IMNMP and INP did not reach statistical significance ($P = 0.0841$; Fig. 4H–M; Table S1). These transcriptional changes are consistent with a shift toward an M1-like program and away from an M2-like program, reinforcing the phenotypic findings.

Immunoblot analysis showed no significant difference in PI3Kγ protein abundance between INP- and IMNMP-treated macrophages ($P = 0.7791$; Fig. 4N, O), whereas the phosphorylated-to-total nuclear factor κB (NF-Kb) p65 ratio was was 1.43 times that in IMNMP-treated cells (Fig. 4N, P), suggesting enhanced NF-κB-associated signaling and providing a potential regulatory basis for the increased expression of inflammatory genes. Further protein analysis showed increased CCAAT/enhancer-binding protein β (C/EBPβ) and inducible nitric oxide synthase (iNOS) abundance, accompanied by reduced arginase 1 abundance (Fig. 4Q–T). The changes in C/EBPβ and NF-κB-associated signaling linked the IMNMP response to transcriptional regulation, while the changes in iNOS and Arg1 supported a shift in macrophage effector-protein expression.

The reprogrammed macrophages released more inflammatory cytokines and T-cell-associated chemokines. Compared with INP treatment, IMNMP increased supernatant concentrations of CXCL9, CXCL10, tumor necrosis factor-α (TNF-α) and IL-12p70 (all $P < 0.0001$; Fig. 4U–X). CXCL9 and IL-12p70 concentrations were 1.61 fold and 2.03 fold the corresponding INP values, respectively. These outputs linked macrophage reprogramming to chemokine signals

associated with T-cell recruitment and cytokines associated with effector activation. The combined phenotypic, transcriptional and secretory changes therefore motivated functional tests of tumor protection and $CD8^+$ T-cell responses.

IMNMP treatment attenuates macrophage-mediated tumor protection and enhances $CD8^+$ T-cell responses

In noncontact Transwell cocultures, TAM-like macrophages treated with *PIK3CG*-targeting small interfering RNA (siRNA) or pretreated with IMNMP reduced Renca-s cell viability compared with untreated TAM-like macrophages, both with and without sunitinib treatment (Fig. 5A). Pik3cg-targeting small interfering RNA and IMNMP pretreatment each lowered Renca-s viability relative to coculture with untreated TAM-like macrophages under both drug conditions (Fig. 5B, S7). With sunitinib, IMNMP-pretreated macrophages produced the lowest tumor-cell viability, reducing the normalized CCK-8 viability signal by 50.7% relative to untreated TAM-like macrophages. These results indicate that inhibiting PI3Kγ in TAM-like macrophages enhances their ability to suppress tumor cell activity and cooperates with sunitinib. The association between genetic disruption and IMNMP treatment suggests that PI3Kγ in macrophages plays a role in tumor protection, prompting researchers to conduct complementary assays on tumor cell apoptosis and proliferation.

Live/dead imaging showed increased propidium iodide (PI) fluorescence in Renca-s cells cocultured with IMNMP-pretreated macrophages compared with Renca-s cells cultured alone or with untreated TAM-like macrophages ($P = 0.0004$ and $P < 0.0001$, respectively; Fig. 5C, D), indicating increased tumor cell death under macrophage coculture. Crystal violet staining further revealed reduced stained-area coverage following coculture with IMNMP-pretreated macrophages (Fig. 5E), consistent with impaired tumor cell survival and proliferation. In direct-contact cocultures, IMNMP pretreatment reduced the overall viability signal of the mixed macrophage–tumor cell population (Fig. 5F, G), showing that the suppressive effect persisted when macrophages and tumor cells were in direct contact rather than separated by a membrane. Imaging of three-dimensional Renca-s spheroids over 3 days revealed a less compact appearance and irregular boundaries in the presence of IMNMP-pretreated macrophages, with CMFDA-labeled macrophages visible in association with the spheroids (Fig. 5H), suggesting that IMNMP-pretreated macrophages can infiltrate spheroids and disrupt their structural integrity. Collectively, these results show that IMNMP-pretreated TAM-like macrophages suppress Renca-s tumor cells across noncontact coculture, direct-contact coculture, and three-dimensional spheroid models, consistent with enhanced macrophage-mediated tumor cell killing.

IMNMP-pretreated macrophages enhanced the expansion and effector output of activated $CD8^+$ T cells. After 72 h of coculture at a macrophage:T-cell ratio of 1:2 under anti-CD3/CD28 stimulation, the CFSE-negative fraction of $CD8^+$ T cells increased from 0.6% with untreated TAM-like macrophages to 72.6% with IMNMP-pretreated macrophages ($P < 0.0001$; Fig. 5I–K). This dilution-based proliferation readout was accompanied by increased granzyme B (GZMB) and interferon-γ (IFN-γ) concentrations in the culture supernatant (both $P < 0.0001$; Fig. 5L, M). GZMB and IFN-γ concentrations reached 9.22 fold and 2.45 fold the levels in untreated-macrophage cocultures, respectively. Macrophage PI3Kγ modulation therefore combined reduced tumor protection with enhanced T-cell proliferation and effector output, supporting evaluation of IMNMP alongside sunitinib in vivo.

IMNMP enhances sunitinib-mediated tumor control in treatment-selected renal tumors

Repeated sunitinib treatment of Renca-s-derived tumors was used to establish the treatment-selected Renca-ris model, with serial bioluminescence imaging showing increased tumor-

associated signals at later treatment stages (Fig. 6A, B), indicating that repeated exposure selected for a tumor population with sustained growth under treatment. Upon subsequent sunitinib challenge, Renca-s-derived tumors continued to grow, whereas tumors derived from parental Renca cells showed reduced growth (Fig. 6C), confirming that the Renca-ris model had acquired a treatment-selected growth advantage rather than merely reflecting residual tumor burden. Multiplex immunofluorescence revealed a higher proportion of $CD68^{+}CD163^{+}$ cells among $CD68^{+}$ macrophages in Renca-ris tumors than in parental Renca tumors (16.05% vs 0.76%; $P = 0.0155$), together with greater PI3Kγ positivity within this $CD68^{+}CD163^{+}$ population (70.26% vs 6.67%; $P = 0.0286$), whereas the overall $CD68^{+}$ cell fraction did not differ significantly ($P = 0.0984$; Fig. 6D–G), showing that the treatment-selected model is characterized by a shift toward $CD163^{+}$ M2-like macrophages with elevated PI3Kγ, rather than by a change in total macrophage abundance.

Formulation delivery improved the activity of IPI-549 and strengthened the response to sunitinib. In the initial comparison with free IPI-549, IMNMP produced greater tumor-associated fluorescence during the 48-h imaging period and smaller, lighter excised tumors (Fig. S8, S9). We then compared untreated controls, sunitinib alone, IMNMP alone and their combination in subcutaneous Renca-ris tumors ($n = 5$ mice per group; Fig. 6H). Sunitinib was given at 20 mg/kg and IMNMP at 10 mg/kg IPI-549 equivalent. The combination produced the greatest suppression of tumor growth, with a day-15 mean tumor volume of 114.1 mm^3, corresponding to reductions of 92.6%, 91.3% and 72.7% relative to the untreated (1533.7 mm^3), sunitinib-alone (1318.8 mm^3) and IMNMP-alone (417.6 mm^3) groups, respectively (Fig. 6I). (Fig. 6I). Notably, the combination was also markedly more effective than IMNMP alone (114.1 vs 417.6 mm^3; 72.7% reduction), the most active single agent. Endpoint tumor mass was lower than with either sunitinib ($P < 0.0001$) or IMNMP ($P = 0.0196$), matching the excised-tumor images (Fig. 6J, K). The improvement over both monotherapies established the therapeutic benefit of the combination and directed attention to the accompanying immune changes.

Combination therapy increased costimulatory and antigen-presentation-associated macrophage phenotypes together with intratumoral $CD8^{+}$ cells. Relative to either monotherapy, sunitinib plus IMNMP increased the fractions of $CD86^{+}$ and major histocompatibility complex class II $(MHC\text{-}II)^{+}$ cells among $F4/80^{+}$ tumor macrophages (Fig. 6L–O and Supplementary Fig. 10). Specifically, the $CD86^{+}$ fraction reached 67.87% with the combination, compared with 54.23% with sunitinib alone and 54.03% with IMNMP alone (33.43% in untreated tumors), whereas the $MHC\text{-}II^{+}$ fraction reached 78.67%, compared with 68.53% and 69.23% for the respective monotherapies (51.00% in untreated tumors). Immunofluorescence staining further showed an increased $CD8^{+}$ cell fraction in the combination group, whereas the corresponding forkhead box P3 $(FOXP3)^{+}$ cell fractions did not differ significantly in the indicated comparisons (Fig. 6P–R), consistent with enhanced $CD8^{+}$ T-cell infiltration without a proportional increase in regulatory T cells. Representative hematoxylin and eosin (H&E) staining of major organs was also performed to assess tissue morphology across treatment groups (Fig. S11). These results indicate that, in the treatment-selected Renca-ris model, combination therapy with sunitinib and IMNMP is superior to either monotherapy. This therapeutic advantage is accompanied by a shift of tumor macrophages toward an M1-like, MHC-II–high phenotype and by increased $CD8^{+}$ T-cell infiltration, whereas the $FOXP3^{+}$ cell fraction remained unchanged. These findings link in vivo efficacy to remodeling of the tumor immune microenvironment.

Sunitinib plus IMNMP is associated with antigen-presentation and effector immune transcriptional programs

Bulk tumor RNA sequencing identified coordinated immune transcriptional changes following combination treatment. Compared with untreated subcutaneous tumors, sunitinib plus IMNMP altered 50 genes at the stated nominal P-value and fold-change thresholds, comprising 39 upregulated and 11 downregulated genes (n = 3 tumors per group; Fig. 7A). Pathway analysis highlighted antigen processing and presentation, cytokine–chemokine signaling and lymphocyte-associated responses (Fig. 7B). The heatmap showed higher relative expression of effector-associated genes including *Cd8a, Prf1* and *Nkg7*, alongside antigen-processing genes including *Psmb8*, *Psmb9*, *Tap1* and *Tap2* (Fig. 7C). *Cxcl9* and *Cd86* linked this response to macrophage activation, while the functional-module map connected selected genes to T-cell activation, MHC-II presentation and chemokine signaling (Fig. 7C, D). This organization of the response around immune functions complemented the cellular phenotypes and led us to quantify enrichment of macrophage and T-cell gene sets.

Gene set enrichment analysis revealed positive enrichment of pro-inflammatory macrophage and effector T-cell signatures in tumors treated with sunitinib plus IMNMP relative to untreated controls (normalized enrichment score (NES) = 1.994, false discovery rate (FDR) = 6.3×10^{-4}; and NES = 2.191, FDR = 6.6×10^{-8}, respectively; Fig. 7E, F). Toll-like receptor signaling was also positively enriched (NES = 1.649, FDR = 0.029; Fig. 7G). These transcriptional patterns were consistent with the increased macrophage CD86 and MHC-II positivity and intratumoral $CD8^+$ cell proportions observed following combination treatment (Fig. 6L–Q).

Collectively, these transcriptomic data show that sunitinib plus IMNMP induces a defined transcriptional response in Renca-ris tumors, characterized by the enrichment of antigen processing/presentation, cytokine–chemokine signaling, pro-inflammatory macrophage, effector T-cell, and Toll-like receptor pathways, and that this transcriptional shift is consistent with the M1-like macrophage and $CD8^+$ T-cell changes observed at the cellular level.

An IMNMP-containing triplet enhances local effector responses in orthotopic renal tumors

We compared sunitinib alone, sunitinib plus BMS-202, sunitinib plus IMNMP and the triplet regimen in orthotopic Renca-ris tumors over 15 days (n = 4 mice per group; Fig. 8A). In a separate distribution experiment, 1,1′-dioctadecyl-3,3,3′,3′-tetramethylindotricarbocyanine iodide (DiR)-labeled IMNMP produced persistent abdominal fluorescence through 72 h, with a distribution distinct from that of DiR-labeled INP at matched tracer doses (Fig. 8B). Serial bioluminescence imaging showed lower tumor-associated signals in the IMNMP-containing groups at later time points, with the triplet group generally showing the weakest signals (Fig. 8C). This imaging response extended the antitumor activity of IMNMP-containing treatment to the renal implantation site and prompted analysis of the local immune response.

The triplet increased intratumoral $CD8^+$ T-cell abundance and effector activity alongside macrophage reprogramming. Tumor macrophages showed higher $CD86^+$ and $MHC\text{-}II^+$ fractions and a lower $CD206^+$ fraction in the triplet group than in the other groups (Fig. S12). The intratumoral $CD8^+$ T-cell fraction was higher in the triplet group than in mice receiving sunitinib alone (P = 0.0235) or sunitinib plus BMS-202 (P = 0.0204; Fig. 8D, F, S13), showing that the triplet increased $CD8^+$ T-cell infiltration beyond these comparator regimens. Compared with sunitinib plus IMNMP, addition of BMS-202 increased the GZMB-positive fraction within $CD3^+CD8^+$ T cells from 33.0% to 46.3% (P = 0.0081) and raised soluble IFN-γ concentrations in tumor-derived samples to 1.2 times the level with sunitinib plus IMNMP (P = 0.0014; Fig. 8E, G, I). The IFN-γ-positive $CD8^+$ fraction was also higher than with sunitinib alone (P = 0.0007; Fig. 8H). The triplet therefore increased both local $CD8^+$ T-cell accumulation and effector output, linking the tumor imaging response to a more active immune compartment.

Serum biochemical measurements showed no statistically significant differences in the indicated comparisons (Fig. 8J–O), indicating that the triplet regimen did not produce detectable systemic biochemical toxicity in these readouts. Representative H&E staining of major organs provided an additional assessment of tissue morphology across treatment groups (Fig. S14). Together with the tumor and immune measurements, these findings characterized the activity and biochemical tolerability of the triplet over the treatment period. We next used single-cell profiling to identify the myeloid transcriptional programs associated with this local immune response.

Single-cell profiling reveals treatment-associated antigen-presentation and interferon-response programs in tumor-associated myeloid cells

Single-cell RNA sequencing of orthotopic tumors from mice treated with sunitinib alone or the triplet regimen (n = 3 mice per group) yielded 41,693 cells after quality control and identified immune, stromal, and renal epithelial populations (Fig. 9A), showing that the dataset captured the major cellular compartments of the orthotopic tumor microenvironment and provided a basis for resolving treatment-associated immune states. Reclustering of the TAM-enriched myeloid compartment (4,115 cells) resolved seven transcriptional states, including macrophage populations characterized by *Mrc1/Cd163*, *Lyve1/Ccl8*, or *Nos2/Cxcl3* expression; *Chil3/Ly6c2*-associated monocytes; and *Dcstamp*-positive, interferon/B-cell activating factor (BAFF)-like, and cycling myeloid populations (Fig. 9B, C), indicating that the myeloid compartment comprised transcriptionally distinct macrophage, monocyte, and cycling states rather than a single uniform population. The interferon/BAFF-like population exhibited expression of Stat1 alongside the antigen-presentation-associated genes H2-Ab1 and Cd74 (Fig. 9C), suggesting that this state combines interferon signaling with an antigen-presentation program.

Mouse-level pseudobulk analysis of the TAM-enriched myeloid compartment revealed positive enrichment of antigen processing and presentation in the triplet group compared with sunitinib alone (NES = 2.053, FDR = 5.17×10^{-4}; Fig. 9D), indicating that the triplet regimen enhanced the antigen-presentation program of tumor-associated myeloid cells. Hallmark gene set analysis further showed positive enrichment of IFN-γ and interferon-α (IFN-α) response signatures (NES = 1.862 and 2.065; FDR = 3.84×10^{-6} and 1.01×10^{-5}, respectively). In contrast, mechanistic target of rapamycin complex 1 (mTORC1) signaling and interleukin-6 (IL-6)–Janus kinase (JAK)–signal transducer and activator of transcription 3 (STAT3) signaling were negatively enriched (NES = −1.888 and −1.563; FDR = 3.13×10^{-6} and 0.0234, respectively). TNF-α signaling via NF-κB also showed positive enrichment (Fig. 9E), further supporting a pro-inflammatory, NF-κB–associated program in the triplet group. These single-cell data show that the triplet regimen reshapes the TAM-enriched myeloid compartment toward transcriptionally distinct states marked by antigen presentation, interferon signaling, and NF-κB–associated pro-inflammatory programs, while mTORC1 and IL-6–JAK–STAT3 signaling are reduced, providing a cellular and pathway-level basis for the immune-microenvironment changes observed in the triplet-treated tumors.

DISCUSSION

Our findings identify PI3Kγ-associated macrophage function as a therapeutically actionable component of the renal cancer microenvironment under sunitinib pressure. Prolonged conditioning by sunitinib-challenged tumor cells generated macrophages that supported tumor cell survival during subsequent drug exposure, whereas genetic PI3Kγ silencing or pharmacological modulation with IMNMP attenuated this protective effect. In vivo, IMNMP combined with sunitinib improved tumor control and was accompanied by increased macrophage costimulatory features and enhanced $CD8^+$ T-cell infiltration. Together, these

observations support a model in which macrophages contribute not only to local immune suppression but also to microenvironmental protection of tumor cells during targeted therapy.

PI3Kγ provides a mechanistic link between these two functions. Previous studies established myeloid PI3Kγ as a regulator of immunosuppressive programs and showed that its inhibition enhances antitumor immunity *(18, 19)*. Our study extends this framework to sunitinib-challenged renal cancer. PI3Kγ-directed macrophage modulation reduced tumor-supportive markers while increasing CD86, iNOS, CXCL9, CXCL10, TNF-α, and IL-12p70, and these changes were accompanied by reduced macrophage-mediated tumor protection and enhanced $CD8^+$ T-cell responses. Increased NF-κB p65 phosphorylation was consistent with this functional shift. By contrast, the role of C/EBPβ remains uncertain because only total protein abundance, rather than transcriptional activity, was measured.

IMNMP was designed to combine PI3Kγ inhibition with protease-responsive and macrophage-associated delivery. Higher MMP-9 abundance in paired renal tumor tissues, MMP-9-induced particle restructuring, increased drug release, and enhanced early macrophage-associated uptake together support the rationale for this design. However, the clinical tissue analysis was limited to three paired specimens, and MMP-9 abundance does not necessarily reflect enzymatic activity. Larger patient cohorts and direct measurements of intratumoral protease activity will be required to determine the translational relevance of this trigger.

Transcriptomic analyses further revealed that macrophage reprogramming extended beyond conventional polarization markers. Bulk profiling showed enrichment of antigen-processing and effector immune programs, whereas single-cell analysis localized prominent antigen-presentation and interferon-response programs to tumor-associated myeloid cells. These findings are consistent with the increased macrophage CD86 and MHC-II expression and enhanced T-cell responses observed experimentally. However, the current data do not establish that macrophage antigen presentation directly drives $CD8^+$ T-cell activation. Antigen-specific presentation assays and functional blockade studies will be needed to test this relationship causally.

Several mechanistic questions remain. Macrophage-specific PI3Kγ perturbation will be required to establish whether macrophages are necessary for the in vivo therapeutic effect, whereas dose-matched free IPI-549 comparisons and cell-resolved biodistribution studies will help define the contribution of the nanocarrier. The BMS-202-containing experiments should also be interpreted cautiously because species-dependent differences in programmed death ligand 1 (PD-L1) binding complicate target attribution in murine tumors.

Overall, our results support a dual therapeutic rationale for macrophage-directed PI3Kγ inhibition in sunitinib-challenged renal cancer. By reducing macrophage-mediated support of tumor cell survival while promoting an immune environment associated with improved T-cell activity, this approach targets two complementary functions of the tumor microenvironment. IMNMP provides a protease-responsive delivery strategy for implementing this intervention and improves tumor control when combined with sunitinib. This work provides a framework for targeting treatment-conditioned macrophage states to reinforce targeted therapy while defining key mechanistic questions for further investigation.

MATERIALS AND METHODS

Study design and experimental units

This study integrated analyses of publicly available datasets and paired human renal tumor and adjacent-tissue specimens with macrophage conditioning, nanocarrier characterization, genetic perturbation, functional coculture assays, and mouse tumor models. The experiments were

designed to investigate whether tumor-conditioned macrophages support tumor cell survival during sunitinib exposure and whether macrophage *PIK3CG* silencing or IMNMP treatment attenuates this protection and alters macrophage-associated immune responses. Separate coculture systems were used to assess macrophage-mediated tumor cell protection and $CD8^+$ T-cell proliferation and effector responses. Subcutaneous and orthotopic renal tumor models were used to evaluate treatment responses and intratumoral immune phenotypes, whereas an experimental pulmonary colonization model assessed tumor growth and survival following intravenous tumor cell inoculation. Bulk tumor RNA sequencing and single-cell RNA sequencing provided complementary analyses of treatment-associated transcriptional changes at the tissue and myeloid-compartment levels, respectively. The experimental units were individual patients for clinical specimens, individual mice for in vivo studies, and independently prepared cell cultures or formulation batches for in vitro experiments. Unless otherwise specified, cell-based and formulation experiments included three independent preparations, and cell viability assays used six technical replicate wells per condition. Measurements from technical wells and microscopic fields were summarized within each independent preparation rather than treated as separate biological replicates. Subcutaneous tumor efficacy experiments included five mice per group, whereas tissue and immune analyses involved three mice per group. Orthotopic efficacy experiments included four mice per group, with three mice per group contributing to immune profiling; single-cell RNA sequencing was performed using three mice per group from the sunitinib-alone and triplet-treated cohorts. In the experimental pulmonary colonization model, lung histology and survival were evaluated in separate cohorts of three and four mice per group, respectively. Following tumor-model establishment, mice were allocated to treatment groups and housing cages. Sample sizes and denominators are reported alongside the corresponding measurements.

Clinical specimens and animals

Between July 3 and July 28, 2026, paired renal tumor and peritumoral tissue samples were collected from three patients undergoing surgery at the Fourth Affiliated Hospital of Soochow University. All patients had previously untreated, histologically confirmed stage I clear-cell RCC, including two T1aN0M0 cases and one T1bN0M0 case. Peritumoral tissues were obtained at least 1 cm from the tumor margin and confirmed to be tumor-free by histopathological examination. Tissue samples were either fixed in 4% paraformaldehyde or stored at −80°C. The study was approved by the institutional ethics committee and conducted in accordance with the Declaration of Helsinki.

Female BALB/c mice aged 6–8 weeks were used for tumor experiments and maintained under specific pathogen-free conditions with unrestricted access to food and water. All animal procedures were approved by the Animal Ethics Committee of the Fourth Affiliated Hospital of Soochow University. Surgical procedures and in vivo imaging were performed under isoflurane anesthesia. Body weight, general health, and tumor burden were monitored throughout the treatment period, and mice reaching predefined humane endpoints were euthanized. Experimental units, group allocation, treatment schedules, and survival follow-up and censoring procedures are described in the corresponding model-specific sections *(33)*.

Cell culture and primary macrophage differentiation

Parental Renca cells were cultured in RPMI-1640 medium supplemented with 10% fetal bovine serum (FBS) and 1% penicillin–streptomycin. RAW264.7 macrophages were maintained in Dulbecco's modified Eagle's medium (DMEM) supplemented with 10% FBS. All cells were cultured at 37°C in a humidified atmosphere containing 5% CO_2. BMDMs were generated from femoral bone marrow isolated from male C57BL/6J mice aged 6–8 weeks. Following erythrocyte lysis, bone marrow cells were seeded at a density of approximately 1×10^6–2×10^6

cells/mL in complete medium supplemented with 20 ng/mL macrophage colony-stimulating factor (M-CSF). Half of the culture medium was replaced on day 3 and every 2–3 days thereafter with fresh M-CSF-supplemented medium. After 6–7 days of differentiation, macrophage enrichment was assessed by F4/80 and CD11b staining. For experiments evaluating formulation responses in primary macrophages, differentiated BMDMs were subsequently conditioned by non-contact coculture with Renca-s cells in a Transwell system for an additional 7 days.

Synthesis and structural characterization of the amphiphiles

The MMP-9-responsive conjugate $mPEG_{10K}$–GPLGVRG–DSPE was synthesized through sequential amide-coupling reactions. N-Hydroxysuccinimide (NHS)-activated $mPEG_{10K}$ (50 mg) was dissolved in 2 mL of chloroform. GPLGVRG peptide (0.9 equivalents), dissolved in ethanol, and triethylamine (3.0 equivalents) were added, and the reaction mixture was stirred at room temperature for 1 h. Subsequently, DSPE–NH_2 (0.9 equivalents) and benzotriazol-1-yloxytripyrrolidinophosphonium hexafluorophosphate (PyBOP; 1.5 equivalents), each separately dissolved in chloroform, were added, and the reaction was continued for an additional 2 h. The solvent was removed under reduced pressure, and the crude product was subjected to three successive purification steps using acetone. The resulting material was dissolved in dimethyl sulfoxide (DMSO), dialyzed against purified water for 12 h using a dialysis membrane with a molecular weight cutoff (MWCO) of 12 kDa, and subsequently lyophilized. The supplier-reported nominal molecular mass of the conjugate was 11,450 ± 200 Da. DSPE–$mPEG_{500}$–M2pep was synthesized via thiol–maleimide conjugation between cysteine-modified M2pep and maleimide-functionalized DSPE–$mPEG_{500}$. Briefly, DSPE–$mPEG_{500}$–maleimide (100 mg) was dissolved in 3 mL of DMSO, followed by the addition of cysteine-modified M2pep (1.1 equivalents) and triethylamine (3.0 equivalents). The reaction mixture was incubated at room temperature for 12 h, dialyzed against purified water for 24 h using a membrane with a MWCO of 2 kDa, and subsequently lyophilized. The M2pep recognition sequence was YEQDPWGVKWWY, with an additional cysteine residue introduced to enable thiol–maleimide conjugation. The peptide precursors and corresponding conjugates were characterized by ^{1}H NMR spectroscopy at 400 MHz in deuterated DMSO-d_6, according to supplier-provided characterization reports. For $mPEG_{10K}$–GPLGVRG–DSPE, the supplier specified a Bruker AVANCE III spectrometer equipped with an autosampler, using 5 mg of sample dissolved in 0.5 mL of solvent. The spectra were examined for peptide-associated downfield resonances, the characteristic PEG methylene signals near δ 3.5 ppm, and lipid-chain resonances near δ 1.2 and 0.85 ppm. Supplier-provided synthetic schemes, individual ^{1}H NMR spectra, and spectral overlays are presented in figs. S2 and S3.

Nanocarrier assembly and component controls

IMNMP was assembled from IPI-549, the MMP-9-responsive conjugate $mPEG_{10K}$–GPLGVRG–DSPE (designated shell 1), and the M2pep-functionalized conjugate DSPE–$mPEG_{500}$–M2pep (designated shell 2). Separate stock solutions of the components in DMSO were combined and introduced into water to induce nanoparticle self-assembly. The resulting dispersion was dialyzed overnight to remove DMSO, and the nanoparticles were recovered using centrifugal ultrafiltration devices with a MWCO of 10 kDa. The purified formulations were stored at 4°C protected from light. To optimize the formulation, shell 1 : shell 2 : IPI-549 proportions of 8.89:1.11:1, 8:2:1, 6.67:3.33:1, and 5:5:1 were evaluated, corresponding to shell 1: shell 2 ratios of approximately 8:1, 4:1, 2:1, and 1:1, respectively. Hydrodynamic diameter and PDI were measured to compare the physicochemical characteristics of the formulations. To distinguish the contributions of the macrophage-recognition and protease-responsive components, three comparator formulations were prepared. IMNP contained the M2pep-functionalized conjugate but lacked the protease-responsive conjugate, whereas INMP retained

the protease-responsive conjugate but lacked the M2pep-functionalized component. INP contained neither functional conjugate and served as the nonfunctionalized nanoparticle control. In the comparator formulations, the omitted functional conjugates were replaced with methoxy-terminated DSPE–mPEG$_{500}$. All formulations were prepared and purified using otherwise identical procedures. IPI-549 content was quantified to match nominal drug concentrations across nanoparticle formulations in cell-based experiments. Fluorescently labeled formulations were purified to remove unincorporated dye and compared under matched tracer-exposure conditions. Three independently prepared formulation batches were analyzed.

For encapsulation efficiency, 10 µL purified suspension was extracted with 490 µL anhydrous methanol. Encapsulation efficiency was calculated as follow:

$$m_{enc} = C_E \times V_{extract} \times \frac{V_s}{V_{aliquot}} \quad (1)$$

$$\text{EE (\%)} = \frac{m_{enc}}{m_{feed}} \times 100 \quad (2)$$

C_E is the HPLC-measured IPI-549 concentration in the extract (µg/mL), $V_{extract}$ = 0.5 mL, $V_{aliquot}$ = 0.010 mL, V_s = 1 mL (final suspension volume), and m_{feed} is the IPI-549 input (µg).

For drug loading, 1 mL purified suspension was lyophilized, weighed (m_{dry}) and extracted with 100 µL anhydrous methanol. Drug loading was calculated as follow:

$$m_{enc,dry} = C_D \times V_{extract,dry} \quad (3)$$

$$\text{DL (\%)} = \frac{m_{enc,dry}}{m_{dry}} \times 100 \quad (4)$$

C_D denote the respective HPLC-measured extract concentrations, $V_{extract,dry}$ = 0.1 mL, and m_{dry} is the mass of lyophilized solids from 1 mL purified suspension (µg).

Physicochemical characterization and enzyme responsiveness

Hydrodynamic diameter and PDI were determined by dynamic light scattering, particle morphology was examined by transmission electron microscopy, and zeta potential was measured by electrophoretic light scattering. Hydrodynamic size measurements reflected the properties of nanoparticles in dispersion, whereas electron microscopy provided morphological information from the imaged particles. The colloidal stability of IMNMP was evaluated by monitoring hydrodynamic diameter and PDI on days 0, 3, 6, 9, 12, 15, and 18 using three independently prepared formulation batches. IPI-549 content was quantified by high-performance liquid chromatography (HPLC). Encapsulation efficiency (%) was calculated as the mass of encapsulated IPI-549 divided by the initial mass of IPI-549 added, multiplied by 100. Drug loading (%) was calculated as the mass of encapsulated IPI-549 divided by the mass of recovered nanoparticles, multiplied by 100. For enzyme-responsiveness assessment, IMNMP suspensions (approximately 0.5 mg/mL total lipid) were incubated with 20 nM MMP-9 in 500 µL of phosphate-buffered saline (PBS, pH 7.4) at 37°C for 2 h. Chromatographic profiles and hydrodynamic size distributions were compared between MMP-9-treated and untreated IMNMP samples to evaluate enzyme-associated changes in formulation properties.

Drug release and chromatographic quantification

For in vitro drug release studies, 500 µL of nanoparticle suspension in PBS was loaded into a dialysis-based release device with 5 mL of external PBS supplemented with 0.1% polysorbate 80. Release experiments were conducted at 37°C in the presence of 1 or 5 nM MMP-9, representing the low- and high-enzyme conditions, respectively. Samples were collected at predetermined time points over 72 h and analyzed by HPLC to quantify released IPI-549.

Chromatographic analysis was performed using a methanol–water mobile phase, a column temperature of 25°C, a flow rate of 1.0 mL/min, an injection volume of 10 μL, and ultraviolet detection at 250 nm. Cumulative IPI-549 release was calculated relative to the amount of drug initially encapsulated in the nanoparticle sample, with correction for drug removed during serial sampling and replacement of the release medium. Assuming a constant external medium volume (V) and equal sampling volumes (v), the cumulative released mass at sampling time n was calculated as:

$$M_n = VC_n + v\sum_{i=1}^{n-1} C_i \quad (5)$$

C_n represents the IPI-549 concentration measured at time n and C_i denotes the concentrations measured at preceding sampling points.

Cumulative release (%) was calculated as:

$$Release\ (\%) = \frac{M_n}{M_0} \times 100 \quad (6)$$

M_0 represents the amount of encapsulated IPI-549 initially loaded into the release device. M_n represents the amount of IPI-549 on the outside of the dialysis bag at the nth time point. MMP-9 measurements in paired tumor and peritumoral tissues provided biological context for the release experiments. Tissue-normalized MMP-9 content (pg/mg) and the enzyme concentrations used in vitro (nM) were treated as distinct quantities *(34, 35)*.

Generation of Renca-s cells and macrophage conditioning

Renca-s cells were established by repeated exposure of parental Renca cells to 3 μM sunitinib. Following each exposure, the sunitinib-containing medium was removed, and surviving cells were allowed to recover and expand in complete medium before reseeding for the subsequent treatment cycle. Selection was continued until cell viability following exposure to 3 μM sunitinib exceeded 75%, after which the selected cells were maintained in medium containing 3 μM sunitinib. Dose–response curves were fitted using a four-parameter logistic model to determine IC_{50} values. The resistance index was calculated as the ratio of the IC_{50} of Renca-s cells to that of parental Renca cells. Macrophage conditioning was performed using 12-well Transwell inserts with 0.4-μm pores, with equal numbers of tumor cells and RAW264.7 macrophages seeded initially. Tumor cells were placed in the upper inserts, whereas macrophages were cultured in the lower wells. For Renca-s-mediated conditioning, culture supernatant collected after sunitinib withdrawal was introduced into the coculture system, without additional sunitinib during the conditioning period. Experimental conditions included unconditioned RAW264.7 macrophages and macrophages cocultured with either parental Renca or Renca-s cells for 12 h or 7 days. Macrophages conditioned with parental Renca cells for 7 days were designated TAM-trend macrophages, whereas those conditioned with Renca-s cells for 7 days were designated TAM-like macrophages. Macrophage phenotypes were assessed by F4/80/CD206 flow cytometry, analysis of Arg1, Mrc1, and Nos2 transcript levels, PI3Kγ protein expression, and measurement of MMP-9, IL-10, and TGF-β concentrations in culture supernatants. For the tumor-support assay, the compartment arrangement was reversed: parental Renca cells were cultured in the lower wells, whereas unconditioned or TAM-like macrophages were placed in the upper inserts, with or without sunitinib treatment.

Formulation uptake and macrophage perturbation

FITC-labeled INP, IMNP, INMP, and IMNMP were incubated with TAM-like macrophages in the Renca-s coculture system. Following incubation, cells were washed and analyzed by flow cytometry to quantify cell-associated FITC fluorescence, with an early assessment

performed at 0.5 h. To evaluate the effect of MMP inhibition, cells were pretreated with 10 μM galardin for 30 min before nanoparticle exposure, and galardin was maintained throughout the incubation period. For cell-selectivity analysis, TAM-like macrophages prelabeled with Cy5 were mixed with unlabeled Renca-s cells at a 1:1 ratio and exposed to FITC-labeled INP or IMNMP for 0.5 or 2 h. Following gating of live singlets, Cy5-prelabeled macrophages were distinguished from unlabeled Renca-s cells, and cell-associated FITC fluorescence was evaluated in each population using unlabeled and single-stained controls. TAM-like macrophages and BMDMs were treated with INP, IMNP, INMP, or IMNMP at matched IPI-549-equivalent concentrations, with untreated cells serving as controls. For subsequent functional coculture assays, macrophages were exposed to the respective formulations for 2 h, washed to remove extracellular formulations, and transferred to fresh medium. For *Pik3cg*-silencing experiments, cells were transfected with *siPik3cg* or *siNC* at a final concentration of 20 nM. Lipid-mediated transfection was performed for 6 h in reduced-serum medium, followed by replacement with complete medium and an additional 48 h of culture. *Pik3cg* transcript levels were subsequently assessed by quantitative polymerase chain reaction (qPCR). For the analysis of formulation-associated soluble factors, culture supernatants were collected at 48 h.

Viability, apoptosis and short-term outgrowth assays

Cell viability was assessed using the Cell Counting Kit-8 (CCK-8) colorimetric assay. Absorbance was measured at 450 nm, and background-corrected values were normalized to the corresponding vehicle-treated or drug-free controls. The same normalization procedure was applied to concentration–response analyses of parental Renca and Renca-s cells. For apoptosis analysis, cells were stained with Annexin V- phycoerythrin (PE) and 7-aminoactinomycin D (7-AAD) and analyzed by flow cytometry. Annexin V-PE-positive/7-AAD-negative events were classified as early apoptotic cells, while double-positive events were classified as cells with impaired membrane function, including those in the late stages of apoptosis. Fluorescence gating and population classification were guided by unstained and single-stained controls *(36)*.

For non-contact functional coculture assays, untreated, *Pik3cg* siRNA-transfected, or IMNMP-pretreated TAM-like macrophages were placed in the upper Transwell inserts (0.4-μm pore size), with Renca-s cells cultured in the lower wells at an initial macrophage-to-tumor cell ratio of 1:1. Cocultures were maintained for 48 h in the presence or absence of 5 μM sunitinib, after which cell viability was assessed in the tumor cell-containing lower compartment. For direct-contact coculture assays, TAM-like macrophages and Renca-s cells were seeded together in 24-well plates at 2×10^5 cells per population (4×10^5 total cells per well) and cultured for 48 h with or without 5 μM sunitinib. Because both cell populations contributed to the colorimetric signal, the CCK-8 readout from direct-contact cocultures represented the combined metabolic activity of macrophages and tumor cells rather than tumor cell-specific viability. Live/dead cell imaging was performed using calcein acetoxymethyl ester (calcein-AM) and propidium iodide, with consistent image acquisition settings across experimental groups. Propidium iodide fluorescence was quantified after background subtraction. For short-term outgrowth assays, cells were harvested using 0.25% trypsin–ethylenediaminetetraacetic acid (EDTA) at 37°C for 2–3 min, collected by centrifugation at 300 × g for 5 min, and reseeded at a density of 500 cells per well. After 48 h of culture, cells were fixed and stained with crystal violet. Short-term outgrowth was quantified as the crystal violet-stained area normalized to the total well area.

Spheroid and $CD8^+$ T-cell cocultures

Renca-s spheroids were generated by seeding 1×10^3 cells per well into low-attachment, round-bottom 96-well plates containing 100 μL of complete medium supplemented with 2% basement membrane matrix. After 3–5 days of spheroid formation, 1×10^4 untreated or IMNMP-pretreated macrophages, prelabeled with 5 μM chloromethylfluorescein diacetate (CMFDA),

were added to each spheroid. The day of macrophage addition was designated day 0. Spheroid morphology and macrophage-associated CMFDA fluorescence were monitored on days 0, 1, 2, and 3. Splenic $CD8^+$ T cells were isolated from BALB/c mice by magnetic separation and labeled with 5 μM CFSE for 10 min at 37°C. CFSE-labeled $CD8^+$ T cells (2×10^5 cells per well) were cocultured with untreated or IMNMP-pretreated TAM-like macrophages (1×10^5 cells per well) for 72 h. T-cell activation was induced using plate-bound anti-CD3 antibodies (5 μg/mL) and soluble anti-CD28 antibodies (2 μg/mL). T-cell proliferation was assessed by CFSE dilution relative to the undivided cell population, while GZMB and IFN-γ concentrations were measured in coculture supernatants. These assays evaluated the effects of macrophage pretreatment on $CD8^+$ T-cell proliferative and effector responses under anti-CD3/CD28 stimulation, independently of tumor cell viability assays.

Flow cytometry and tumor immune profiling

Cells were resuspended in PBS containing 2% FBS and 2 mM EDTA. Following Fc receptor blocking, surface staining was performed for 30 min at 4°C. For intracellular staining, cells were fixed and permeabilized before incubation with the corresponding antibodies. Flow cytometric analysis of immune-cell populations was performed after exclusion of debris, doublets, and nonviable cells. Single-stained controls were used for fluorescence compensation. The percentage of marker-positive cells was calculated relative to the corresponding parent population, with consistent gating denominators across treatment groups for each comparison *(36)*.

CD206 expression in conditioned RAW264.7 macrophages was assessed by flow cytometry. Following nanoparticle treatment, CD86 positivity was evaluated within $F4/80^+$ RAW264.7 macrophages and $CD45^+CD11b^+$ BMDMs. Tumor tissues were enzymatically dissociated with 1 mg/mL collagenase IV and 100 μg/mL deoxyribonuclease I (DNase I) at 37°C for 30 min, and the resulting cell suspensions were passed through a 70-μm cell strainer. Tumor-associated macrophages were identified as $CD11b^+F4/80^+$ cells within viable $CD45^+$ singlets, and CD86 and MHC-II positivity were quantified within this population. $CD3^+CD8^+$ T cells were quantified as a fraction of $CD45^+$ cells, whereas GZMB and IFN-γ positivity were assessed within the $CD3^+CD8^+$ T-cell population. For intracellular cytokine staining, cells were restimulated for 4 h with 50 ng/mL phorbol ester, 500 ng/mL ionomycin, and 10 μg/mL brefeldin A. CD206 positivity was additionally assessed within the tumor-associated macrophage population in orthotopic tumors. Samples from individual mice were processed and analyzed separately, without inter-animal pooling.

qPCR and immunoblotting

RNA was extracted from harvested macrophages, and 1 μg of RNA was reverse-transcribed into complementary DNA (cDNA). The expression levels of *Arg1*, *Mrc1*, *Nos2*, *Tnf*, *Cxcl9*, *Cxcl10*, and *Pik3cg* were quantified by qPCR, with each sample analyzed in technical triplicate. Technical replicates were summarized within each independent macrophage culture before statistical analysis. The comparative Ct method was applied under the assumption of comparable amplification efficiencies between the target and reference genes *(37, 38)*.

Proteins were extracted using lysis buffer supplemented with protease and phosphatase inhibitors. Equal amounts of protein were separated by sodium dodecyl sulfate–polyacrylamide gel electrophoresis, transferred onto membranes, and detected by chemiluminescence. The proteins analyzed included PI3Kγ, total NF-κB p65, NF-κB p65 phosphorylated at Ser536, C/EBPβ, Arg1, and iNOS. Immunoblot bands were quantified by densitometric analysis after background subtraction. Target protein levels were normalized to the corresponding loading control, either GAPDH or β-tubulin, whereas phosphorylated p65 was normalized to total p65.

Normalized band intensities were expressed relative to the corresponding control group, with consistent normalization procedures applied across samples within each comparison.

Soluble mediators and tissue analysis

Clarified culture supernatants were analyzed using sandwich enzyme-linked immunosorbent assays (ELISAs). MMP-9, IL-10, and TGF-β concentrations were measured following macrophage conditioning; CXCL9, CXCL10, TNF-α, and IL-12p70 concentrations were measured after nanoparticle treatment; and GZMB and IFN-γ concentrations were measured after 72 h of T-cell coculture. Analyte concentrations were determined from the corresponding standard curves, corrected for sample dilution where applicable, and expressed in pg/mL. Soluble IFN-γ concentrations were also quantified in tumor-derived samples collected from the orthotopic tumor experiments. For tissue MMP-9 quantification, clinical specimens were weighed and homogenized in ice-cold PBS at a tissue-to-buffer ratio of 1:9. The homogenates were centrifuged at 10,000 × g for 10 min at 4°C, and the resulting supernatants were analyzed for MMP-9 by ELISA in duplicate. Tissue-normalized MMP-9 content was calculated as $C \times D \times V/m$, where C represents the measured MMP-9 concentration (pg/mL), D is the sample dilution factor, V is the total homogenate volume (mL), and m is the tissue wet mass (mg). Results were expressed as picograms of MMP-9 per milligram of wet tissue (pg/mg). Fixed tissue specimens were paraffin-embedded and sectioned at a thickness of 4 μm by a commercial histology service. Multiplex immunofluorescence staining was performed to assess CD68, CD163, and PI3Kγ expression for macrophage characterization, as well as CD8 or FOXP3 expression for immune-cell infiltration analysis. Colocalization was assessed within the relevant cell populations, and marker-positive fractions were calculated using the corresponding reference populations. Specifically, the proportions of $CD68^+$, $CD8^+$, and $FOXP3^+$ cells were calculated relative to the total number of nucleated cells. Measurements from multiple microscopic fields were aggregated to obtain a single value for each patient or mouse. H&E staining was performed to evaluate tissue morphology. Pulmonary tumor area was quantified as a percentage of the total analyzed lung-tissue area.

Renca-ris induction and subcutaneous treatment

To establish the Renca-ris model, 2×10^6 Renca-s cells suspended in 100 μL PBS were injected subcutaneously into the right flank of mice. When tumors reached approximately 100 mm^3, sunitinib treatment was initiated by oral gavage at 20 mg/kg in repeated cycles of three consecutive dosing days followed by two treatment-free days, continuing through day 28 of the induction period. Tumor bioluminescence was monitored longitudinally during induction. Tumor-derived material collected after the induction period was designated Renca-ris. Tumor fragments of approximately 2 mm^3 were subsequently reimplanted subcutaneously, and tumors derived from parental Renca cells served as comparators for evaluating tumor growth during sunitinib exposure. For the subcutaneous efficacy study, mice bearing Renca-ris tumors were assigned to four groups: untreated control, sunitinib, IMNMP, and sunitinib plus IMNMP (n = 5 per group). Treatment was initiated when tumor volumes reached approximately 100 mm^3, designated as day 0. Sunitinib was administered by oral gavage at 20 mg/kg on days 0–2, 5–7, and 10–12. IMNMP was administered intravenously at an IPI-549-equivalent dose of 10 mg/kg once daily from day 0 through day 14. Tumor dimensions were measured on days 0, 3, 6, 9, 12, and 15, and tumor volume was calculated as length × $width^2/2$. At the experimental endpoint, tumors were excised and weighed, and tissue specimens were collected for immune phenotyping, tissue analysis, and bulk RNA sequencing. A separate efficacy comparison between free IPI-549 and IMNMP evaluated endpoint tumor weights, with five excised tumors reported for each group.

Orthotopic tumors and fluorescence imaging

Renca-ris-derived tumor material was implanted into the left renal cortex of anesthetized mice to establish orthotopic tumors. Following tumor establishment, mice were assigned to four treatment groups (n = 4 per group): sunitinib, sunitinib plus BMS-202, sunitinib plus IMNMP, and sunitinib plus IMNMP plus BMS-202. Sunitinib was administered by oral gavage at 20 mg/kg, IMNMP intravenously at an IPI-549-equivalent dose of 10 mg/kg, and BMS-202 intraperitoneally at 20 mg/kg. Pretreatment measurements on day 0 served as the baseline. Sunitinib was administered on days 0–2, 5–7, and 10–12, consistent with the subcutaneous treatment schedule, whereas IMNMP and BMS-202 were administered once daily on days 0–14 in their respective treatment groups. Tumor bioluminescence was monitored on days 0, 3, 6, 9, 12, and 15. Three mice per group were included in tumor immune profiling, and three mice from each of the sunitinib and triple-combination groups were included in single-cell RNA sequencing. In vivo fluorescence distribution was evaluated in a separate cohort of five mice per group. DiR-labeled IMNMP or INP was administered intravenously at matched fluorescent tracer doses, and fluorescence images were acquired at 0, 3, 6, 12, 24, 48, and 72 h. Fluorescence signals within defined tumor regions of interest were quantified after background subtraction using consistent image acquisition settings. For bioluminescence imaging, mice bearing luciferase-expressing Renca-derived tumors received intraperitoneal D-luciferin (150 mg/kg), and images were acquired 10 min after administration. Bioluminescence was quantified as total photon flux within defined regions of interest, with longitudinal measurements normalized to each animal's baseline where applicable. Missing longitudinal observations were not imputed. In a separate fluorescence distribution experiment involving subcutaneous tumor-bearing mice, groups designated IMNMP and IPI-549 were imaged at 0, 3, 6, 12, 24, and 48 h. Ex vivo fluorescence imaging was also performed on excised hearts, livers, spleens, lungs, kidneys, and tumors to evaluate the anatomical distribution of fluorescent signals.

Pulmonary colonization, survival and safety

To establish an experimental pulmonary colonization model, Renca-ris tumors were dissociated into viable single-cell suspensions, and 5×10^5 cells suspended in 100 μL PBS were injected intravenously via the tail vein. Treatment was initiated 10 days after tumor cell inoculation, designated as treatment day 0, and continued through the treatment period ending on day 15. Mice received either sunitinib alone (20 mg/kg, oral gavage) or sunitinib combined with IMNMP (10 mg/kg, IPI-549 equivalent, intravenously) and BMS-202 (20 mg/kg, intraperitoneally). Separate animal cohorts were used for lung histopathological analysis (n = 3 per group) and survival assessment (n = 4 per group). Survival time was calculated from the date of tumor cell inoculation, and mice were followed until death, euthanasia at a humane endpoint, or study completion on post-inoculation day 60. Animals alive at study completion were right-censored at their last follow-up. At the experimental endpoint, serum biochemical parameters, including alanine aminotransferase (ALT), aspartate aminotransferase (AST), albumin (ALB), blood urea nitrogen (BUN), creatine kinase (CK), and total protein (TP), were measured. Histopathological examination was performed on the heart, liver, spleen, lungs, and non-tumor-bearing right kidney. The tumor-bearing left kidney was collected separately for tumor-related analyses.

Public datasets and bulk transcriptomic analysis

Publicly available RCC transcriptomic datasets included GSE65615, GSE68629, GSE281304, GSE273886, E-MTAB-3267, and GSE212525. These datasets encompassed sunitinib-associated cohorts and studies involving neoadjuvant axitinib, neoadjuvant cabozantinib, and sitravatinib with or without nivolumab; dataset provenance and cohort characteristics are summarized in table S2 *(39–43)*. Gene expression data were normalized using platform-appropriate procedures and summarized at the gene level. *PIK3CG* expression was examined

across tissue samples and annotated cell populations, and its associations with macrophage-related expression signatures were assessed using Spearman's rank correlation. Single-sample gene-set enrichment analysis was used to characterize macrophage-associated transcriptional signatures. For patient-level comparisons, repeated specimens were summarized within individual patients to avoid treating multiple samples from the same patient as independent observations. Cell populations in publicly available single-cell datasets were annotated based on normalized expression of established marker genes. Bulk RNA sequencing was performed on subcutaneous tumors from untreated mice and mice treated with sunitinib plus IMNMP, with three independent tumors analyzed per group. Sample-level gene expression matrices were subjected to principal component analysis, differential expression analysis, and gene-set enrichment analysis. Log_2 fold changes were calculated relative to the untreated group, such that positive values indicated higher gene expression in the combination-treatment group. Gene-set enrichment analysis assessed whether genes belonging to predefined pathways were preferentially concentrated toward either end of the treatment-associated ranked gene list *(44, 45)*. Nominal pathway P values were reported separately from multiple-testing-adjusted significance measures.

Single-cell and mouse-level myeloid analyses

Single-cell RNA sequencing was performed on orthotopic tumors from three mice treated with sunitinib alone and three mice receiving the triple combination of sunitinib, IMNMP, and BMS-202. After data processing, 41,693 cells were retained, comprising 10,635, 7,012, and 5,141 cells from the three sunitinib-treated mice and 8,132, 4,420, and 6,353 cells from the three triple-combination-treated mice, respectively. Major cell populations were annotated based on marker-gene expression and visualized using uniform manifold approximation and projection (UMAP). A TAM-enriched myeloid compartment was extracted from global clusters 2 and 9 by retaining cells expressing at least two of the following markers: *Lyz2*, *Adgre1*, *Csf1r*, *Cd68*, *Fcgr1*, *Tyrobp*, *Lst1*, and *Aif1*. The selected cells were reclustered using the SCTransform (SCT) assay, with 2,000 variable features and 30 principal components. The first 25 principal components were used for neighbor identification and visualization, with a clustering resolution of 0.45 *(46)*. The TAM-enriched myeloid compartment comprised 4,115 cells and was resolved into seven transcriptional states: *Mrc1*/*Cd163* TAMs, *Lyve1*/*Ccl8* TAMs, *Nos2*/*Cxcl3* TAMs, *Chil3*/*Ly6c2* monocytes, *Dcstamp*-positive myeloid cells, interferon/BAFF-like myeloid cells, and cycling myeloid cells. Differential expression and pathway enrichment analyses were performed using mouse-level pseudobulk profiles generated from the combined myeloid compartment, with each mouse treated as an independent biological replicate *(47)*. For pseudobulk aggregation, gene counts from the retained cells were summed within each mouse before between-group comparisons. The triple-combination group was compared with the sunitinib-alone group, with positive NES values indicating enrichment in the triple-combination group. Hallmark and Kyoto Encyclopedia of Genes and Genomes (KEGG) gene sets were evaluated *(44, 45)*, and nominal and multiple-testing-adjusted P values were reported separately.

Statistical analysis

Technical replicates were summarized within independent experimental units before statistical testing. Data are presented as mean ± standard deviation unless otherwise indicated. Two-group comparisons were performed using two-sided paired or unpaired Student's t tests, as appropriate. Comparisons involving multiple groups were conducted using one-way or two-way analysis of variance, followed by Tukey's or Bonferroni-adjusted multiple comparisons, respectively. Nonparametric comparisons were performed using the Wilcoxon signed-rank, Mann–Whitney U, or Kruskal–Wallis test, as appropriate, with Dunn's correction for multiple comparisons following the Kruskal–Wallis test. Longitudinal data were analyzed by evaluating

treatment and time while accounting for repeated measurements within individual animals. Missing observations were not imputed. Survival was analyzed using the Kaplan–Meier method, and survival distributions were compared using the log-rank test. A two-sided P value < 0.05 was considered nominally significant. For transcriptomic analyses, multiple-testing correction was performed using the Benjamini–Hochberg procedure, and adjusted P values were distinguished from nominal P values.

References

1. B. I. Rini, E. R. Plimack, V. Stus, R. Gafanov, T. Waddell, D. Nosov, F. Pouliot, B. Alekseev, D. Soulières, B. Melichar, I. Vynnychenko, S. Jobim de Azevedo, D. Borchiellini, R. S. McDermott, J. Bedke, S. Tamada, S. Wu, J. Markensohn, Y. Zhang, A. Loboda, A. Vajdi, R. F. Perini, J. Burgents, T. Powles, Pembrolizumab plus axitinib versus sunitinib for advanced clear cell renal cell carcinoma: 5-year survival and biomarker analyses of the phase 3 KEYNOTE-426 trial. Nat. Med. 31, 3475–3484 (2025). doi: 10.1038/s41591-025-03867-5.

2. R. J. Motzer, C. Porta, M. Eto, T. Powles, V. Grünwald, T. E. Hutson, B. Alekseev, S. Y. Rha, J. Merchan, J. C. Goh, A.-K. A. Lalani, U. De Giorgi, B. Melichar, S.-H. Hong, H. Gurney, M. J. Méndez-Vidal, E. Kopyltsov, S. Tjulandin, T. Alonso Gordoa, V. Kozlov, A. Alyasova, E. Winquist, P. Maroto, M. Kim, A. Peer, G. Procopio, T. Takagi, S. Wong, J. Bedke, M. Schmidinger, K. Rodriguez-Lopez, J. Burgents, C. He, C. E. Okpara, J. McKenzie, T. K. Choueiri, CLEAR Trial Investigators, Lenvatinib Plus Pembrolizumab Versus Sunitinib in First-Line Treatment of Advanced Renal Cell Carcinoma: Final Prespecified Overall Survival Analysis of CLEAR, a Phase III Study. J. Clin. Oncol. 42, 1222–1228 (2024). doi: 10.1200/JCO.23.01569.

3. R. J. Motzer, T. Powles, M. Burotto, B. Escudier, M. T. Bourlon, A. Y. Shah, C. Suárez, A. Hamzaj, C. Porta, C. M. Hocking, E. R. Kessler, H. Gurney, Y. Tomita, J. Bedke, J. Zhang, B. Simsek, C. Scheffold, A. B. Apolo, T. K. Choueiri, Nivolumab plus cabozantinib versus sunitinib in first-line treatment for advanced renal cell carcinoma (CheckMate 9ER): long-term follow-up results from an open-label, randomised, phase 3 trial. Lancet Oncol. 23, 888–898 (2022). doi: 10.1016/S1470-2045(22)00290-X.

4. N. M. Tannir, L. Albigès, D. F. McDermott, M. Burotto, T. K. Choueiri, H. J. Hammers, P. Barthélémy, E. R. Plimack, C. Porta, S. George, F. Donskov, M. B. Atkins, H. Gurney, C. K. Kollmannsberger, M.-O. Grimm, C. Barrios, Y. Tomita, D. Castellano, V. Grünwald, B. I. Rini, R. Jiang, H. Desilva, V. Fedorov, C.-W. Lee, R. J. Motzer, Nivolumab plus ipilimumab versus sunitinib for first-line treatment of advanced renal cell carcinoma: extended 8-year follow-up results of efficacy and safety from the phase III CheckMate 214 trial. Ann. Oncol. 35, 1026–1038 (2024). doi: 10.1016/j.annonc.2024.07.727.

5. R. J. Motzer, L. Albiges, S. A. Treviño Aguirre, R. Kanesvaran, P. Centkowski, M. A. Reimers, J. P. Sade, D. Pouessel, E. Biscaldi, E. Esteban, J. Á. Arranz Arija, S. S. Tykodi, M. van Kooten Losio, A. Dighe, H. Ma, V. Valmeekam, A. Simmons, C. Scheffold, S. Andrianova, D. A. Braun, T. Powles, T. K. Choueiri, Cabozantinib plus nivolumab and ipilimumab in previously untreated, advanced renal cell carcinoma: final results and biomarker analyses from the phase III COSMIC-313 study. Ann. Oncol. 37, 861–871 (2026). doi: 10.1016/j.annonc.2026.02.011.

6. D. A. Braun, K. Street, K. P. Burke, D. L. Cookmeyer, T. Denize, C. B. Pedersen, S. H. Gohil, N. Schindler, L. Pomerance, L. Hirsch, Z. Bakouny, Y. Hou, J. Forman, T. Huang, S.

Li, A. Cui, D. B. Keskin, J. Steinharter, G. Bouchard, M. Sun, E. M. Pimenta, W. Xu, K. M. Mahoney, B. A. McGregor, M. S. Hirsch, S. L. Chang, K. J. Livak, D. F. McDermott, S. A. Shukla, L. R. Olsen, S. Signoretti, A. H. Sharpe, R. A. Irizarry, T. K. Choueiri, C. J. Wu, Progressive immune dysfunction with advancing disease stage in renal cell carcinoma. Cancer Cell 39, 632–648.e8 (2021). doi: 10.1016/j.ccell.2021.02.013.

7. A. Obradovic, N. Chowdhury, S. M. Haake, C. Ager, V. Wang, L. Vlahos, X. V. Guo, D. H. Aggen, W. K. Rathmell, E. Jonasch, J. E. Johnson, M. Roth, K. E. Beckermann, B. I. Rini, J. McKiernan, A. Califano, C. G. Drake, Single-cell protein activity analysis identifies recurrence-associated renal tumor macrophages. Cell 184, 2988–3005.e16 (2021). doi: 10.1016/j.cell.2021.04.038.

8. C. Krishna, R. G. DiNatale, F. Kuo, R. M. Srivastava, L. Vuong, D. Chowell, S. Gupta, C. Vanderbilt, T. A. Purohit, M. Liu, E. Kansler, B. G. Nixon, Y.-B. Chen, V. Makarov, K. A. Blum, K. Attalla, S. Weng, M. L. Salmans, M. Golkaram, L. Liu, S. Zhang, R. Vijayaraghavan, T. Pawlowski, V. Reuter, M. I. Carlo, M. H. Voss, J. Coleman, P. Russo, R. J. Motzer, M. O. Li, C. S. Leslie, T. A. Chan, A. A. Hakimi, Single-cell sequencing links multiregional immune landscapes and tissue-resident T cells in ccRCC to tumor topology and therapy efficacy. Cancer Cell 39, 662–677.e6 (2021). doi: 10.1016/j.ccell.2021.03.007.

9. R. Li, J. R. Ferdinand, K. W. Loudon, G. S. Bowyer, S. Laidlaw, F. Muyas, L. Mamanova, J. B. Neves, L. Bolt, E. S. Fasouli, A. R. J. Lawson, M. D. Young, Y. Hooks, T. R. W. Oliver, T. M. Butler, J. N. Armitage, T. Aho, A. C. P. Riddick, V. Gnanapragasam, S. J. Welsh, K. B. Meyer, A. Y. Warren, M. G. B. Tran, G. D. Stewart, I. Cortés-Ciriano, S. Behjati, M. R. Clatworthy, P. J. Campbell, S. A. Teichmann, T. J. Mitchell, Mapping single-cell transcriptomes in the intra-tumoral and associated territories of kidney cancer. Cancer Cell 40, 1583–1599.e10 (2022). doi: 10.1016/j.ccell.2022.11.001.

10. L. Kinget, S. Naulaerts, J. Govaerts, I. Vanmeerbeek, J. Sprooten, R. S. Laureano, N. Dubroja, G. Shankar, F. M. Bosisio, E. Roussel, A. Verbiest, F. Finotello, M. Ausserhofer, D. Lambrechts, B. Boeckx, A. Wozniak, L. Boon, J. Kerkhofs, J. Zucman-Rossi, M. Albersen, M. Baldewijns, B. Beuselinck, A. D. Garg, A spatial architecture-embedding HLA signature to predict clinical response to immunotherapy in renal cell carcinoma. Nat. Med. 30, 1667–1679 (2024). doi: 10.1038/s41591-024-02978-9.

11. K. Bi, M. X. He, Z. Bakouny, A. Kanodia, S. Napolitano, J. Wu, G. Grimaldi, D. A. Braun, M. S. Cuoco, A. Mayorga, L. DelloStritto, G. Bouchard, J. Steinharter, A. K. Tewari, N. I. Vokes, E. Shannon, M. Sun, J. Park, S. L. Chang, B. A. McGregor, R. Haq, T. Denize, S. Signoretti, J. L. Guerriero, S. Vigneau, O. Rozenblatt-Rosen, A. Rotem, A. Regev, T. K. Choueiri, E. M. Van Allen, Tumor and immune reprogramming during immunotherapy in advanced renal cell carcinoma. Cancer Cell 39, 649–661.e5 (2021). doi: 10.1016/j.ccell.2021.02.015.

12. Z. Long, C. Sun, M. Tang, Y. Wang, J. Ma, J. Yu, J. Wei, J. Ma, B. Wang, Q. Xie, J. Wen, Single-cell multiomics analysis reveals regulatory programs in clear cell renal cell carcinoma. Cell Discov. 8, 68 (2022). doi: 10.1038/s41421-022-00415-0.

13. N. J. Salgia, A. Khan, W. M. Aubrecht, G. C. Twoey, J. Chow, K. Attwood, H. Yu, J. L. Chiello, N. Hansen, B. J. Wasik, B. D. Mercier, H. Ebrahimi, L. Meza, O. Maguire, M. Mastri, C. Whalen, H. Minderman, P. Pirrotte, S. Byron, E. A. Repasky, P. K. Singh, W. Bshara, J.

Wang, A. J. R. McGray, S. I. Abrams, B. Xu, K. H. Eng, M. D. Long, S. K. Pal, E. C. Kauffman, J. B. Muhitch, Comprehensive tumor-immune profiling reveals mediators of paradoxical immune sensitivity in sarcomatoid renal cell carcinoma. Cancer Cell 43, 2014–2033.e9 (2025). doi: 10.1016/j.ccell.2025.07.010.

14. C. Kalogirou, M. Krebs, A. S. Kunz, O. Hahn, H. Kübler, M. Schwinger, A. Hartmann, A. Schmieder, M. Eckstein, Spatial transcriptomic profiling of metastatic renal cell carcinoma identifies chemokine-driven macrophage and CD8+ T-cell interactions predictive of immunotherapy response. J. Immunother. Cancer 13, e012991 (2025). doi: 10.1136/jitc-2025-012991.

15. Q. Ge, J. Meng, Z. Wang, A. Anwaier, J. Lu, X. Tian, Y. Wang, J. Yang, H. Zhang, D. Ye, W. Xu, Spatially segregated APOE+ macrophages restrict immunotherapy efficacy in clear cell renal cell carcinoma. Theranostics 15, 5312–5336 (2025). doi: 10.7150/thno.109097.

16. W. Jiang, L. Liu, Z. Xu, Y. Qiu, B. Zhang, J. Cheng, J. Luo, Y. Qu, J. Guo, J. Xu, SPP1+ Tumor-Associated Macrophages Drive Immunotherapy Resistance via CD8+ T-cell Dysfunction in Clear-Cell Renal Cell Carcinoma. Cancer Immunol. Res. 13, 1533–1546 (2025). doi: 10.1158/2326-6066.CIR-24-1146.

17. J. Chen, J. Mo, J. Wei, M. Qu, J. Dai, Y. Kong, H. Xu, J. Li, X. Yan, C. Cui, L. Si, Z. Chi, J. Guo, X. Wu, X. Sheng, MARCO+ Tumor-Associated Macrophages Impede CD8+ T Cell Immunity to Facilitate Immunotherapy Resistance in Renal Cell Carcinoma. Adv. Sci. 12, e14600 (2025). doi: 10.1002/advs.202514600.

18. M. M. Kaneda, K. S. Messer, N. Ralainirina, H. Li, C. J. Leem, S. Gorjestani, G. Woo, A. V. Nguyen, C. C. Figueiredo, P. Foubert, M. C. Schmid, M. Pink, D. G. Winkler, M. Rausch, V. J. Palombella, J. Kutok, K. McGovern, K. A. Frazer, X. Wu, M. Karin, R. Sasik, E. E. W. Cohen, J. A. Varner, PI3Kγ is a molecular switch that controls immune suppression. Nature 539, 437–442 (2016). doi: 10.1038/nature19834.

19. O. De Henau, M. Rausch, D. Winkler, L. F. Campesato, C. Liu, D. H. Cymerman, S. Budhu, A. Ghosh, M. Pink, J. Tchaicha, M. Douglas, T. Tibbitts, S. Sharma, J. Proctor, N. Kosmider, K. White, H. Stern, J. Soglia, J. Adams, V. J. Palombella, K. McGovern, J. L. Kutok, J. D. Wolchok, T. Merghoub, Overcoming resistance to checkpoint blockade therapy by targeting PI3Kγ in myeloid cells. Nature 539, 443–447 (2016). doi: 10.1038/nature20554.

20. C. A. Evans, T. Liu, A. Lescarbeau, S. J. Nair, L. Grenier, J. A. Pradeilles, Q. Glenadel, T. Tibbitts, A. M. Rowley, J. P. DiNitto, E. E. Brophy, E. L. O'Hearn, J. A. Ali, D. G. Winkler, S. I. Goldstein, P. O'Hearn, C. M. Martin, J. G. Hoyt, J. R. Soglia, C. Cheung, M. M. Pink, J. L. Proctor, V. J. Palombella, M. R. Tremblay, A. C. Castro, Discovery of a Selective Phosphoinositide-3-Kinase (PI3K)-γ Inhibitor (IPI-549) as an Immuno-Oncology Clinical Candidate. ACS Med. Chem. Lett. 7, 862–867 (2016). doi: 10.1021/acsmedchemlett.6b00238.

21. D. S. Hong, M. Postow, B. Chmielowski, R. Sullivan, A. Patnaik, E. E. W. Cohen, G. Shapiro, C. Steuer, M. Gutierrez, H. Yeckes-Rodin, R. Ilaria, B. O'Connell, J. Peng, G. Peng, N. Zizlsperger, A. Tolcher, J. D. Wolchok, Eganelisib, a First-in-Class PI3Kγ Inhibitor, in Patients with Advanced Solid Tumors: Results of the Phase 1/1b MARIO-1 Trial. Clin. Cancer Res. 29, 2210–2219 (2023). doi: 10.1158/1078-0432.ccr-22-3313.

22. B. C. O'Connell, C. Hubbard, N. Zizlsperger, D. Fitzgerald, J. L. Kutok, J. Varner, R. Ilaria,

Jr., M. A. Cobleigh, D. Juric, K. H. R. Tkaczuk, A. Elias, A. Lee, S. Dakhil, E. Hamilton, H. Soliman, S. Peluso, Eganelisib combined with immune checkpoint inhibitor therapy and chemotherapy in frontline metastatic triple-negative breast cancer triggers macrophage reprogramming, immune activation and extracellular matrix reorganization in the tumor microenvironment. J. Immunother. Cancer 12, e009160 (2024). doi: 10.1136/jitc-2024-009160.

23. E. Blanco, H. Shen, M. Ferrari, Principles of nanoparticle design for overcoming biological barriers to drug delivery. Nat. Biotechnol. 33, 941–951 (2015). doi: 10.1038/nbt.3330.

24. M. Cieslewicz, J. Tang, J. L. Yu, H. Cao, M. Zavaljevski, K. Motoyama, A. Lieber, E. W. Raines, S. H. Pun, Targeted delivery of proapoptotic peptides to tumor-associated macrophages improves survival. Proc. Natl. Acad. Sci. U.S.A. 110, 15919–15924 (2013). doi: 10.1073/pnas.1312197110.

25. C. Ngambenjawong, H. H. Gustafson, J. M. Pineda, N. A. Kacherovsky, M. Cieslewicz, S. H. Pun, Serum stability and affinity optimization of an M2 macrophage-targeting peptide (M2pep). Theranostics 6, 1403–1414 (2016). doi: 10.7150/thno.15394.

26. Y. Sun, M. F. Cronin, M. C. P. Mendonça, J. Guo, C. M. O'Driscoll, M2pep-Modified Cyclodextrin-siRNA Nanoparticles Modulate the Immunosuppressive Tumor Microenvironment for Prostate Cancer Therapy. Mol. Pharm. 20, 5921–5936 (2023). doi: 10.1021/acs.molpharmaceut.3c00769.

27. Y. Chen, L. Gong, Y. Cao, Z. Liu, Y. Wang, H. Cheng, Y. Feng, S. Yao, Y. Yin, Z. Wu, Z. Huang, Reprogramming tumor-associated macrophages by a dually targeted milk exosome system as a potent monotherapy for cancer. J. Control. Release 366, 395–409 (2024). doi: 10.1016/j.jconrel.2023.12.058.

28. Y. Jiang, D. Nie, Z. Hu, C. Zhang, L. Chang, Y. Li, Z. Li, W. Hu, H. Li, S. Li, C. Xu, S. Liu, F. Yang, W. Wen, D. Han, K. Zhang, W. Qin, Macrophage-Derived Nanosponges Adsorb Cytokines and Modulate Macrophage Polarization for Renal Cell Carcinoma Immunotherapy. Adv. Healthcare Mater. 13, e2400303 (2024). doi: 10.1002/adhm.202400303.

29. Y. Cao, B. Qiao, Q. Chen, Z. Xie, X. Dou, L. Xu, H. Ran, L. Zhang, Z. Wang, Tumor microenvironment remodeling via targeted depletion of M2-like tumor-associated macrophages for cancer immunotherapy. Acta Biomater. 160, 239–251 (2023). doi: 10.1016/j.actbio.2023.02.006.

30. J. Li, Z. Ge, S. Liu, PEG-sheddable polyplex micelles as smart gene carriers based on MMP-cleavable peptide-linked block copolymers. Chem. Commun. 49, 6974–6976 (2013). doi: 10.1039/c3cc43576h.

31. Y. He, X. Tian, X. Fan, X. Gong, S. Tan, A. Pan, S. Liang, H. Xu, F. Zhou, Enzyme-Triggered Size-Switchable Nanosystem for Deep Tumor Penetration and Hydrogen Therapy. ACS Appl. Mater. Interfaces 15, 552–565 (2023). doi: 10.1021/acsami.2c18184.

32. Z. Xiao, Y. Tan, Y. Cai, J. Huang, X. Wang, B. Li, L. Lin, Y. Wang, X. Shuai, K. Zhu, Nanodrug removes physical barrier to promote T-cell infiltration for enhanced cancer immunotherapy. J. Control. Release 356, 360–372 (2023). doi: 10.1016/j.jconrel.2023.02.029.

33. N. Percie du Sert, V. Hurst, A. Ahluwalia, S. Alam, M. T. Avey, M. Baker, W. J. Browne,

A. Clark, I. C. Cuthill, U. Dirnagl, M. Emerson, P. Garner, S. T. Holgate, D. W. Howells, N. A. Karp, S. E. Lazic, K. Lidster, C. J. MacCallum, M. Macleod, E. J. Pearl, O. H. Petersen, F. Rawle, P. Reynolds, K. Rooney, E. S. Sena, S. D. Silberberg, T. Steckler, H. Würbel, The ARRIVE guidelines 2.0: Updated guidelines for reporting animal research. PLOS Biol. 18, e3000410 (2020). doi: 10.1371/journal.pbio.3000410.

34. S. Bhattacharjee, DLS and zeta potential – What they are and what they are not? J. Control. Release 235, 337–351 (2016). doi: 10.1016/j.jconrel.2016.06.017.

35. J. Shen, D. J. Burgess, In vitro dissolution testing strategies for Nanoparticulate Drug Delivery Systems: Recent developments and challenges. Drug Deliv. Transl. Res. 3, 409–415 (2013). doi: 10.1007/s13346-013-0129-z.

36. A. Cossarizza, H. D. Chang, A. Radbruch, S. Abrignani, R. Addo, M. Akdis, I. Andrä, F. Andreata, F. Annunziato, E. Arranz, P. Bacher, S. Bari, V. Barnaba, J. Barros-Martins, D. Baumjohann, C. G. Beccaria, D. Bernardo, D. A. Boardman, J. Borger, C. Böttcher, L. Brockmann, M. Burns, D. H. Busch, G. Cameron, I. Cammarata, A. Cassotta, Y. Chang, F. G. Chirdo, E. Christakou, L. Čičin-Šain, L. Cook, A. J. Corbett, R. Cornelis, L. Cosmi, M. S. Davey, S. De Biasi, G. De Simone, G. Del Zotto, M. Delacher, F. Di Rosa, J. Di Santo, A. Diefenbach, J. Dong, T. Dörner, R. J. Dress, C.-A. Dutertre, S. B. G. Eckle, P. Eede, M. Evrard, C. S. Falk, M. Feuerer, S. Fillatreau, A. Fiz-Lopez, M. Follo, G. A. Foulds, J. Fröbel, N. Gagliani, G. Galletti, A. Gangaev, N. Garbi, J. A. Garrote, J. Geginat, N. A. Gherardin, L. Gibellini, F. Ginhoux, D. I. Godfrey, P. Gruarin, C. Haftmann, L. Hansmann, C. M. Harpur, A. C. Hayday, G. Heine, D. C. Hernández, M. Herrmann, O. Hoelsken, Q. Huang, S. Huber, J. E. Huber, J. Huehn, M. Hundemer, W. Y. K. Hwang, M. Iannacone, S. M. Ivison, H.-M. Jäck, P. K. Jani, B. Keller, N. Kessler, S. Ketelaars, L. Knop, J. Knopf, H.-F. Koay, K. Kobow, K. Kriegsmann, H. Kristyanto, A. Krueger, J. F. Kuehne, H. Kunze-Schumacher, P. Kvistborg, I. Kwok, D. Latorre, D. Lenz, M. K. Levings, A. C. Lino, F. Liotta, H. M. Long, E. Lugli, K. N. MacDonald, L. Maggi, M. K. Maini, F. Mair, C. Manta, R. A. Manz, M.-F. Mashreghi, A. Mazzoni, J. McCluskey, H. E. Mei, F. Melchers, S. Melzer, D. Mielenz, L. Monin, L. Moretta, G. Multhoff, L. E. Muñoz, M. Muñoz-Ruiz, F. Muscate, A. Natalini, K. Neumann, L. G. Ng, A. Niedobitek, J. Niemz, L. N. Almeida, S. Notarbartolo, L. Ostendorf, L. J. Pallett, A. A. Patel, G. I. Percin, G. Peruzzi, M. Pinti, A. G. Pockley, K. Pracht, I. Prinz, I. Pujol-Autonell, N. Pulvirenti, L. Quatrini, K. M. Quinn, H. Radbruch, H. Rhys, M. B. Rodrigo, C. Romagnani, C. Saggau, S. Sakaguchi, F. Sallusto, L. Sanderink, I. Sandrock, C. Schauer, A. Scheffold, H. U. Scherer, M. Schiemann, F. A. Schildberg, K. Schober, J. Schoen, W. Schuh, T. Schüler, A. R. Schulz, S. Schulz, J. Schulze, S. Simonetti, J. Singh, K. M. Sitnik, R. Stark, S. Starossom, C. Stehle, F. Szelinski, L. Tan, A. Tarnok, J. Tornack, T. I. M. Tree, J. J. P. van Beek, W. van de Veen, K. van Gisbergen, C. Vasco, N. A. Verheyden, A. von Borstel, K. A. Ward-Hartstonge, K. Warnatz, C. Waskow, A. Wiedemann, A. Wilharm, J. Wing, O. Wirz, J. Wittner, J. H. M. Yang, J. Yang, Guidelines for the use of flow cytometry and cell sorting in immunological studies (third edition). Eur. J. Immunol. 51, 2708–3145 (2021). doi: 10.1002/eji.202170126.

37. S. A. Bustin, J. M. Ruijter, M. J. B. van den Hoff, M. Kubista, M. W. Pfaffl, G. L. Shipley, N. Tran, S. Rödiger, A. Untergasser, R. Mueller, T. Nolan, M. Milavec, M. J. Burns, J. F. Huggett, J. Vandesompele, C. T. Wittwer, MIQE 2.0: Revision of the Minimum Information for Publication of Quantitative Real-Time PCR Experiments Guidelines. Clin. Chem. 71, 634–

651 (2025). doi: 10.1093/clinchem/hvaf043.

38. K. J. Livak, T. D. Schmittgen, Analysis of relative gene expression data using real-time quantitative PCR and the 2(-Delta Delta C(T)) Method. Methods 25, 402–408 (2001). doi: 10.1006/meth.2001.1262.

39. M. A. Bilen, B. T. Vo, Y. Liu, R. Greenwald, A. H. Davarpanah, D. McGuire, R. Shiradkar, L. Li, A. Midya, B. Nazha, J. T. Brown, S. Williams, W. Session, G. Russler, S. Caulfield, S. S. Joshi, V. M. Narayan, C. P. Filson, K. Ogan, O. Kucuk, B. C. Carthon, L. Del Balzo, A. Cohen, A. Boyanton, N. Prokhnevska, M. A. Cardenas, E. Sobierajska, C. S. Jansen, D. H. Patil, E. Nicaise, A. O. Osunkoya, H. T. Kissick, V. A. Master, Neoadjuvant cabozantinib for locally advanced nonmetastatic clear cell renal cell carcinoma: a phase 2 trial. Nat. Cancer 6, 432–444 (2025). doi: 10.1038/s43018-025-00922-5.

40. R. Wray, H. Paverd, I. Machado, J. Barbieri, F. Easita, A. R. Edwards, F. A. Gallagher, I. A. Mendichovszky, T. J. Mitchell, M. de la Roche, J. D. Shields, S. Ursprung, L. Wallis, A. Y. Warren, S. J. Welsh, M. Crispin-Ortuzar, G. D. Stewart, J. O. Jones, NAXIVA Study Group, Angiogenic and immune predictors of neoadjuvant axitinib response in renal cell carcinoma with venous tumour thrombus. Nat. Commun. 16, 3870 (2025). doi: 10.1038/s41467-025-58436-8.

41. J. A. Karam, P. Msaouel, C. L. Haymaker, S. F. Matin, M. T. Campbell, A. J. Zurita, A. Y. Shah, I. I. Wistuba, E. Marmonti, D. Y. Duose, E. R. Parra, L. M. Solis Soto, C. Laberiano-Fernandez, M. Lozano, A. Abraham, M. Hallin, C. D. Chin, P. Olson, H. Der-Torossian, X. Yan, N. M. Tannir, C. G. Wood, Phase II trial of neoadjuvant sitravatinib plus nivolumab in patients undergoing nephrectomy for locally advanced clear cell renal cell carcinoma. Nat. Commun. 14, 2684 (2023). doi: 10.1038/s41467-023-38342-7.

42. B. Beuselinck, S. Job, E. Becht, A. Karadimou, V. Verkarre, G. Couchy, N. Giraldo, N. Rioux-Leclercq, V. Molinié, M. Sibony, R. Elaidi, C. Teghom, J.-J. Patard, A. Méjean, W. H. Fridman, C. Sautès-Fridman, A. de Reyniès, S. Oudard, J. Zucman-Rossi, Molecular subtypes of clear cell renal cell carcinoma are associated with sunitinib response in the metastatic setting. Clin. Cancer Res. 21, 1329–39 (2015). doi: 10.1158/1078-0432.CCR-14-1128.

43. G. D. Stewart, F. C. O'Mahony, A. Laird, L. Eory, A. L. Lubbock, A. Mackay, J. Nanda, M. O'Donnell, P. Mullen, S. A. McNeill, A. C. P. Riddick, D. Berney, A. Bex, M. Aitchison, I. M. Overton, D. J. Harrison, T. Powles, Sunitinib Treatment Exacerbates Intratumoral Heterogeneity in Metastatic Renal Cancer. Clin. Cancer Res. 21, 4212–23 (2015). doi: 10.1158/1078-0432.CCR-15-0207.

44. A. S. Castanza, J. M. Recla, D. Eby, H. Thorvaldsdóttir, C. J. Bult, J. P. Mesirov, Extending support for mouse data in the Molecular Signatures Database (MSigDB). Nat. Methods 20, 1619–1620 (2023). doi: 10.1038/s41592-023-02014-7.

45. M. Kanehisa, M. Furumichi, Y. Sato, M. Kawashima, M. Ishiguro-Watanabe, KEGG for taxonomy-based analysis of pathways and genomes. Nucleic Acids Res. 51, D587–D592 (2023). doi: 10.1093/nar/gkac963.

46. S. Choudhary, R. Satija, Comparison and evaluation of statistical error models for scRNA-seq. Genome Biol. 23, 27 (2022). doi: 10.1186/s13059-021-02584-9.

47. J. W. Squair, M. Gautier, C. Kathe, M. A. Anderson, N. D. James, T. H. Hutson, R. Hudelle,

T. Qaiser, K. J. E. Matson, Q. Barraud, A. J. Levine, G. La Manno, M. A. Skinnider, G. Courtine, Confronting false discoveries in single-cell differential expression. Nat. Commun. 12, 5692 (2021). doi: 10.1038/s41467-021-25960-2.

Acknowledgments

Funding:

This work was supported by the Health Talent Support Program of Suzhou Industrial Park (Grant No. YQWS202513), the National Natural Science Foundation of China (Grant No. 82572292), Prof. Changgeng Ruan's Research and Innovation Fund for Graduate Students of the First Affiliated Hospital of Soochow University (Grant No. RSJCX202601), the Natural Science Foundation of Jiangsu Province (BK20241796), the National Natural Science Foundation of China (82672588), and the Postgraduate Research & Practice Innovation Program of Jiangsu Province (Grant No. 26CXJH5950).

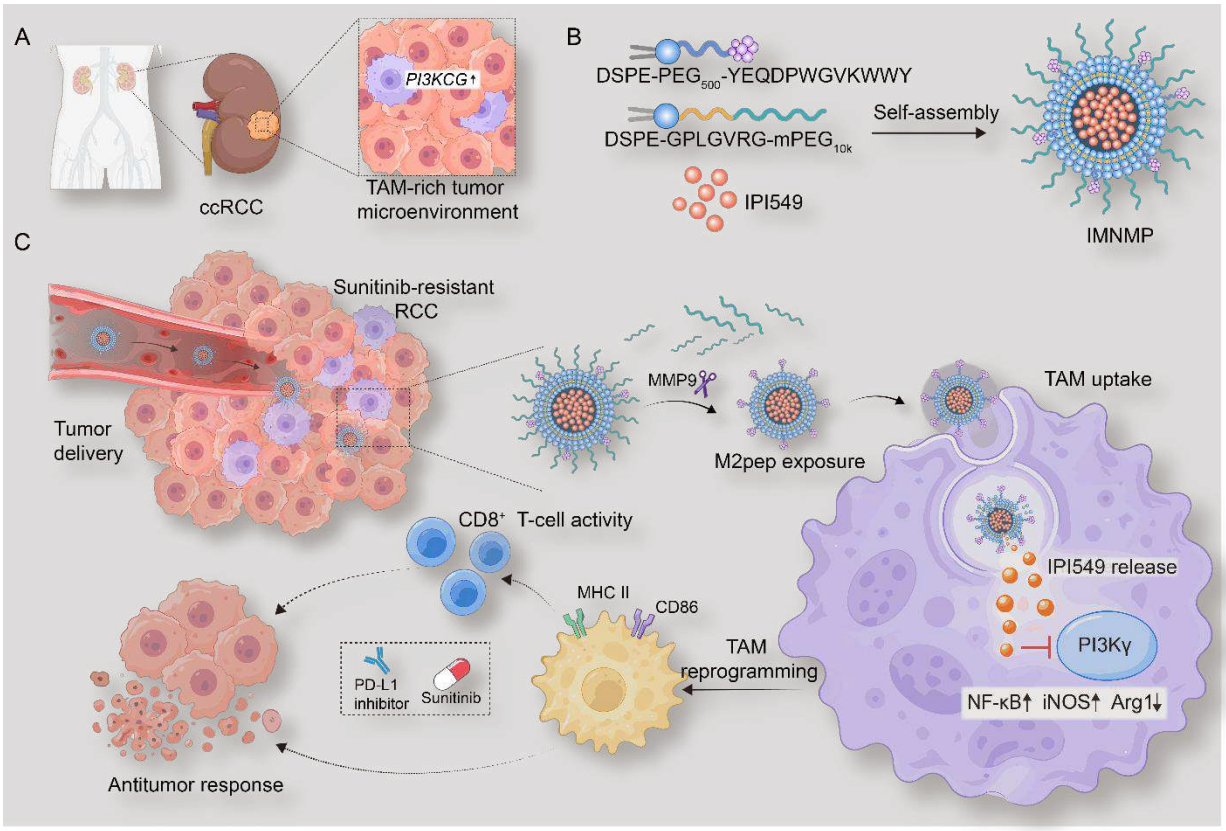
Author contributions:

Conceptualization: ZXH, XRH, XY; Methodology: AGZ, XC, YFH, JGJ; Investigation: ZXH, XRH, XY; Data curation: ZXH, XRH, XY; Formal analysis: AGZ, XC, YFH, JGJ; Visualization: ZXH; Supervision: XDW, HW, HJ, YHH, HBX, DJ, JQH; Writing&original draft: ZXH; Writing&review & editing: ZXH, XRH, XY, XDW, HW, HJ, YHH, HBX, DJ, JQH.

Competing interests: Authors declare that they have no competing interests.

Data and materials availability: All data are available in the main text or the supplementary materials.

Figures and Tables



Scheme 1. PI3Kγ Inhibition Reprograms Tumor-Associated Macrophages in Renal Cell Carcinoma

(A) PI3Kγ is highly expressed in patient renal tumor tissue. (B) Schematic diagram of IMNMP nano-self-assembly. (C) Mechanism by which IMNMP reprograms tumor-associated macrophages in renal cell carcinoma in vivo.

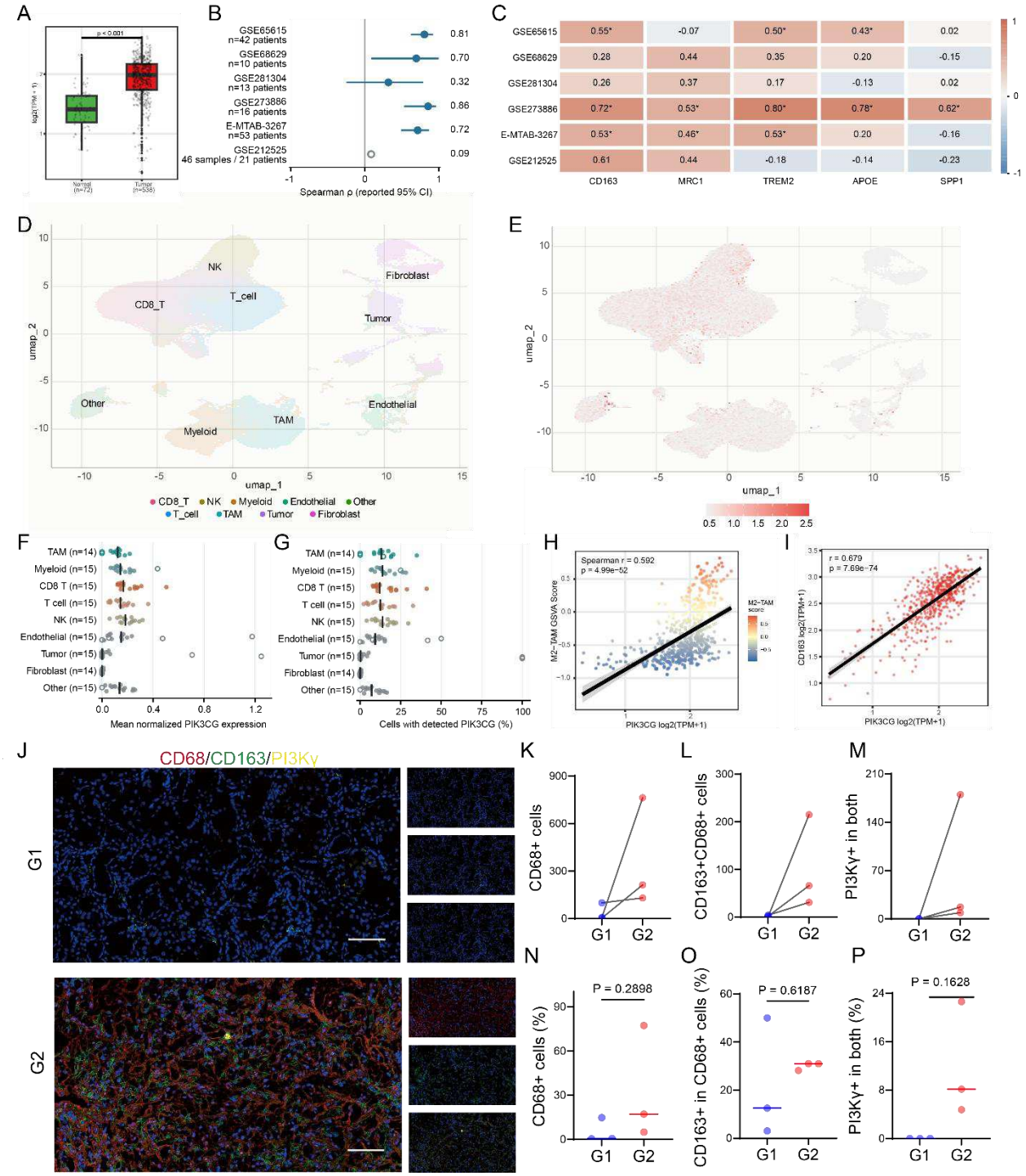


Fig. 1. PIK3CG expression associates with immune and macrophage features in renal cancer

(A) *PIK3CG* expression in normal kidney (n = 72) and renal tumor (n = 538) transcriptomes. (B) Spearman correlations between *PIK3CG* expression and macrophage-associated gene signatures across six RCC cohorts. Points indicate correlation coefficients, with 95% confidence intervals shown where available. Cohort sample sizes are indicated. (C) Correlations of *PIK3CG* expression with CD163, MRC1, TREM2, APOE, and SPP1 across the six datasets. (D) Uniform Manifold Approximation and Projection (UMAP) of cells from the public single-cell RNA-sequencing dataset, colored by annotated cell type. (E) Distribution of *PIK3CG* expression across the UMAP embedding. (F and G) Mean normalized PIK3CG expression (F) and the percentage of cells with detectable *PIK3CG* expression (G) across

annotated cell populations. Individual sample measurements and sample numbers are shown. (H) Spearman correlation between *PIK3CG* expression and the macrophage signature score ($r = 0.592$, $P = 4.99 \times 10^{-52}$). (I) Spearman correlation between PIK3CG and CD163 expression ($r = 0.679$, $P = 7.69 \times 10^{-74}$). (J) Representative multiplex immunofluorescence images of CD68, CD163, and PI3Kγ in paired peritumoral kidney (G1) and renal tumor (G2) tissues (Bar = 100 μm), with nuclear counterstaining. (K to M) Quantification of $CD68^+$ cells (K), $CD68^+CD163^+$ cells (L), and $PI3K\gamma^+$ cells within the $CD68^+CD163^+$ population (M). (N to P) Corresponding percentages of $CD68^+$ cells among nucleated cells (N), $CD163^+$ cells among $CD68^+$ cells (O), and $PI3K\gamma^+$ cells among $CD68^+CD163^+$ cells (P). Tissue analyses included three paired specimens (n = 3 patients), with one data point per patient in each group. Lines in (K) to (M) connect paired specimens. Exact P values for the comparisons in (N) to (P) are indicated in the corresponding panels.

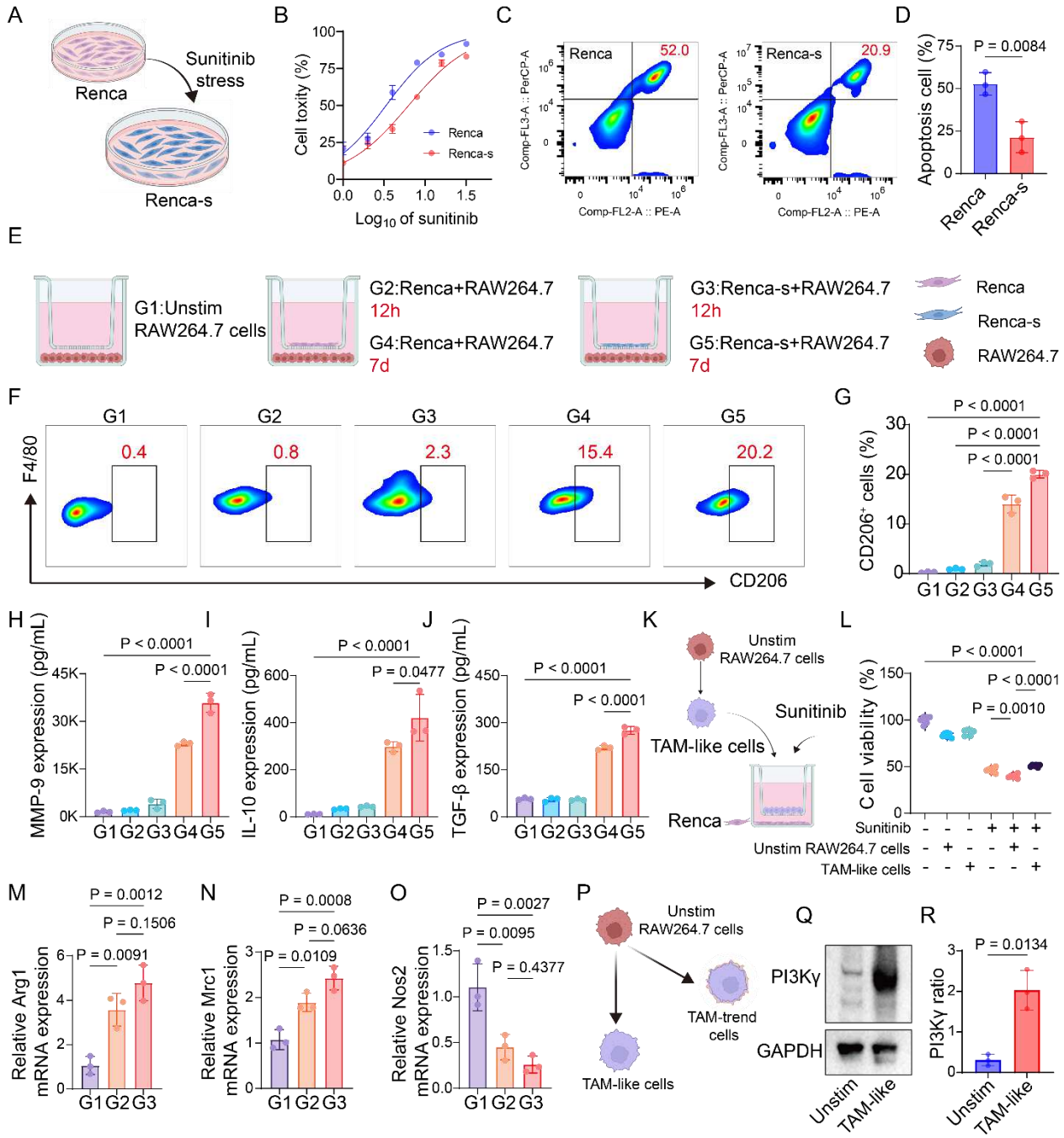
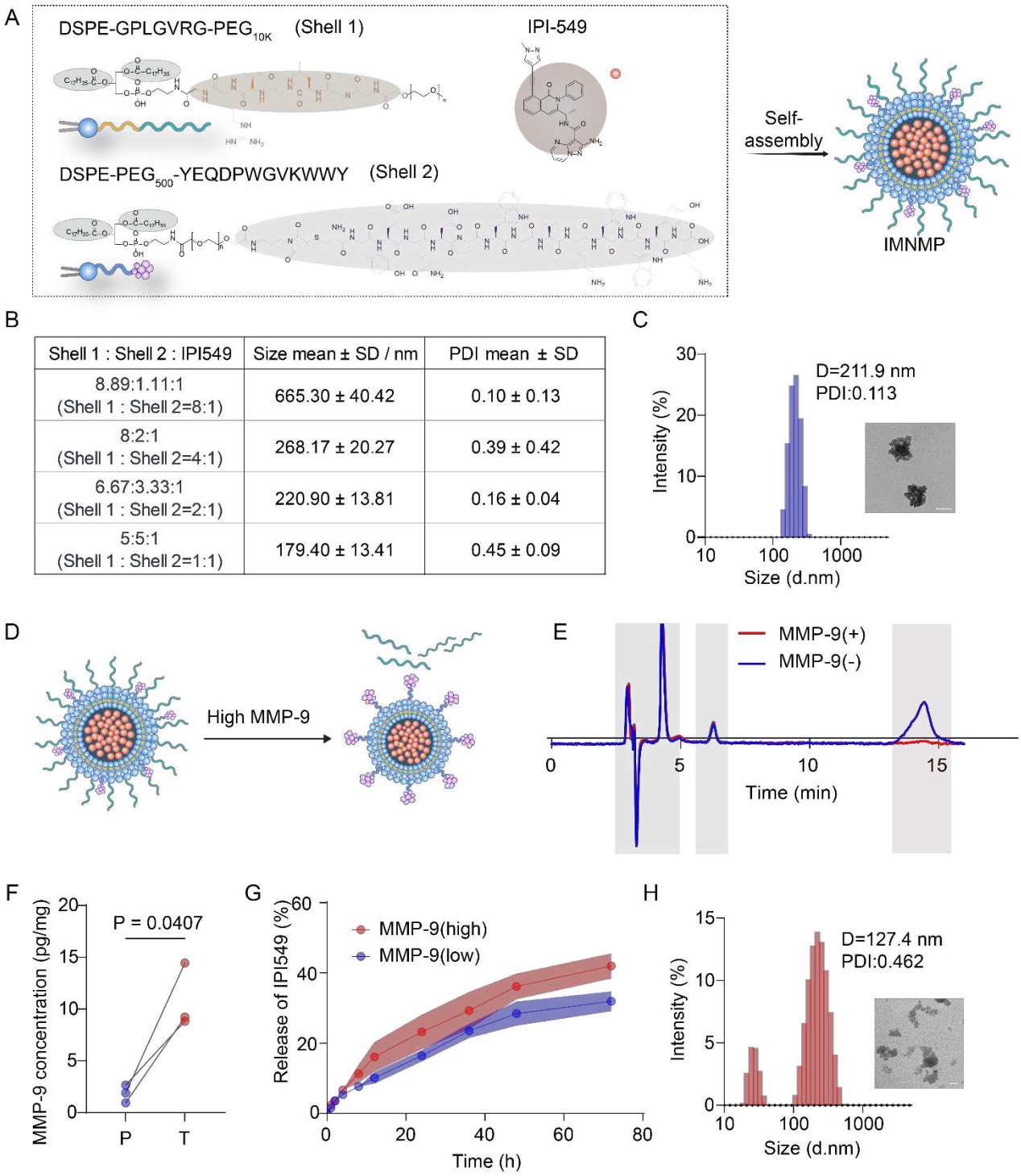


Fig. 2. Prolonged exposure to sunitinib-conditioned renal cancer cells generates tumor-supportive macrophages

(A) Schematic illustration of the generation of sunitinib-selected Renca cells (Renca-s) through repeated sunitinib exposure. (B) Sunitinib dose–response curves for parental Renca and Renca-s cells. (C and D) Representative flow cytometry plots (C) and quantification (D) of apoptosis in parental Renca and Renca-s cells following sunitinib treatment. (E) Schematic of the noncontact coculture model used for macrophage conditioning: G1, unconditioned RAW264.7 macrophages; G2, macrophages cocultured with parental Renca cells for 12 h; G3, macrophages cocultured with Renca-s cells for 12 h; G4, macrophages cocultured with parental Renca cells for 7 days; and G5, macrophages cocultured with Renca-s cells for 7 days. (F and G) Representative flow cytometry plots of F4/80 and CD206 staining (F) and quantification of $CD206^+$ cell proportions (G) across the five conditioning groups. (H to J) Concentrations of

MMP-9 (H), interleukin-10 (IL-10; I), and transforming growth factor-β (TGF-β; J) in culture supernatants. (K and L) Schematic of the macrophage-mediated tumor protection assay (K) and Renca cell viability (L) under the indicated coculture conditions, with or without sunitinib treatment. (M to O) Relative mRNA levels of Arg1 (M), Mrc1 (N), and Nos2 (O) in unconditioned macrophages (G1), macrophages conditioned with parental Renca cells for 7 days (G2, TAM-trend), and macrophages conditioned with Renca-s cells for 7 days (G3, TAM-like). (P) Schematic illustrating the generation of TAM-trend and TAM-like macrophages through 7-day coculture with parental Renca and Renca-s cells, respectively. (Q and R) Representative immunoblot analysis of PI3Kγ and GAPDH (Q) and quantification of PI3Kγ protein abundance normalized to GAPDH (R) in unconditioned and TAM-like macrophages. Cell-based experiments included three independent preparations, and viability assays included six technical replicate wells per condition, as detailed in Materials and Methods. Data are presented as mean ± SD with individual measurements where applicable. P values are indicated for the corresponding comparisons.



Shell 1 : Shell 2 : IPI549	Size mean ± SD / nm	PDI mean ± SD
8.89:1.11:1 (Shell 1 : Shell 2=8:1)	665.30 ± 40.42	0.10 ± 0.13
8:2:1 (Shell 1 : Shell 2=4:1)	268.17 ± 20.27	0.39 ± 0.42
6.67:3.33:1 (Shell 1 : Shell 2=2:1)	220.90 ± 13.81	0.16 ± 0.04
5:5:1 (Shell 1 : Shell 2=1:1)	179.40 ± 13.41	0.45 ± 0.09

Fig. 3. Design, physicochemical characterization, and MMP-9 responsiveness of IMNMP
(A) Schematic illustration of IMNMP self-assembly from the PI3Kγ inhibitor IPI-549, the MMP-9–responsive lipid conjugate mPEG10K–GPLGVRG–DSPE, and the M2pep-functionalized lipid conjugate DSPE–PEG500–M2pep. (B) Hydrodynamic diameters and polydispersity indices (PDIs) of formulations prepared at the four indicated component ratios. (C) Representative dynamic light scattering (DLS) size distribution and transmission electron microscopy (TEM) image of the selected IMNMP formulation. (Bar = 200 nm). (D) Schematic illustration of the proposed MMP-9–mediated cleavage of the responsive linker, resulting in shedding of the long PEG chains and increased exposure of M2pep. (E) Chromatographic profiles of IMNMP before and after incubation with 20 nM MMP-9. (F) MMP-9 levels in paired peritumoral kidney (P) and renal tumor (T) tissues from three patients, normalized to

tissue mass. Lines connect matched specimens from the same patient (n = 3 pairs). (G) Cumulative IPI-549 release from IMNMP over 72 h under low (1 nM) and high (5 nM) MMP-9 conditions. (H) Representative DLS size distribution and TEM image of IMNMP following MMP-9 treatment. (Bar = 50 nm). Formulation measurements were obtained from three independent preparations. Data in (B) are presented as mean ± SD.

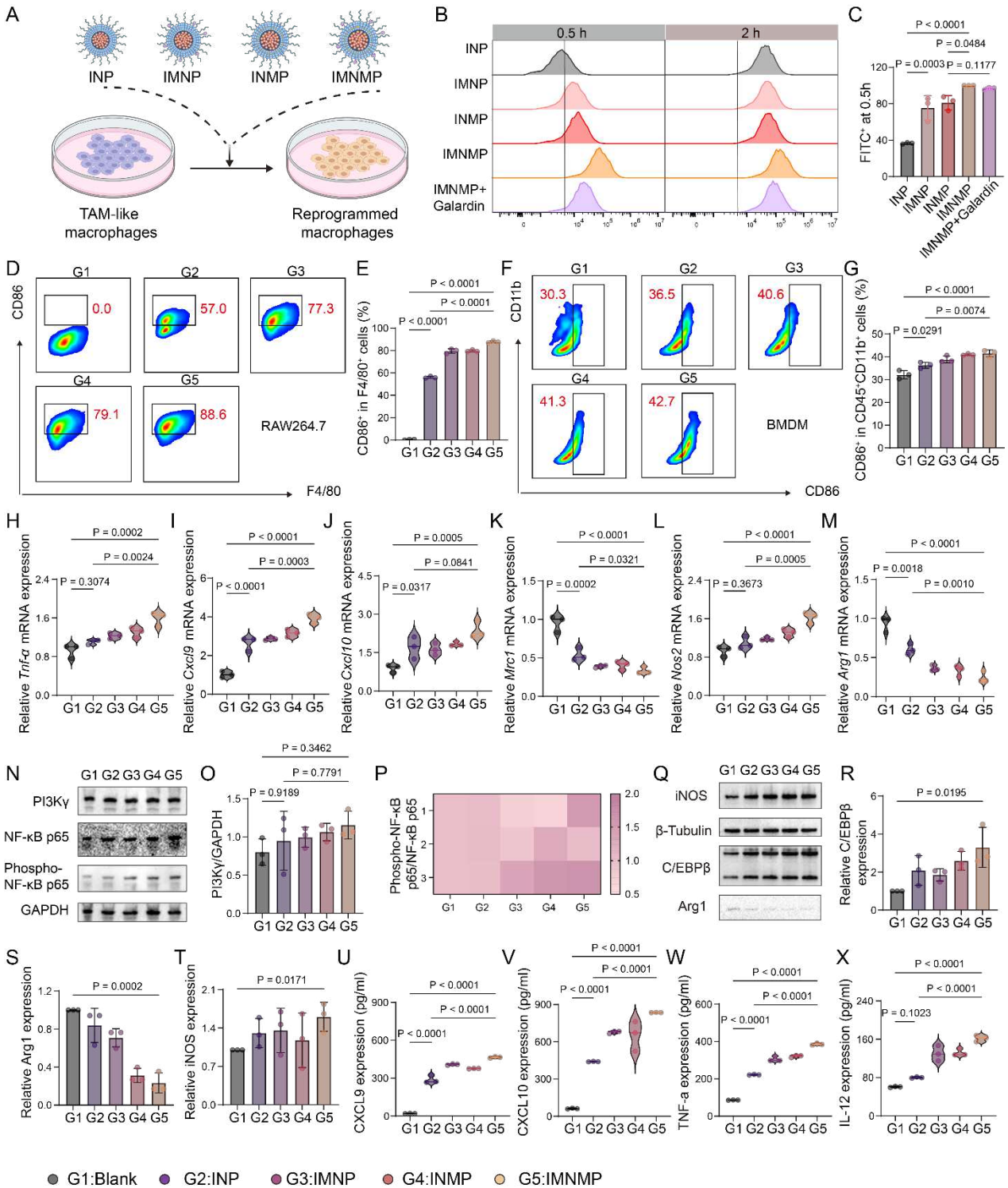


Fig. 4. IMNMP enhances macrophage-associated fluorescence and promotes an immunostimulatory phenotype

(A) Schematic illustration of the formulation controls and macrophage treatment. INP lacks both functional components, IMNP contains M2pep but lacks the MMP-9–responsive component, INMP contains the MMP-9–responsive component but lacks M2pep, and IMNMP contains both functional components. (B) Representative flow cytometry histograms showing cell-associated FITC fluorescence after exposure to the indicated formulations, including IMNMP in the presence of the matrix metalloproteinase inhibitor galardin. (C) Quantification of FITC-positive TAM-like macrophages after 0.5 h of formulation exposure. (D and E)

Representative flow cytometry plots of F4/80 and CD86 expression (D) and quantification of $CD86^+$ cells among $F4/80^+$ RAW264.7-derived TAM-like macrophages (E). (F and G) Representative flow cytometry plots (F) and quantification of $CD86^+$ cells among $CD45^+CD11b^+$ bone marrow-derived macrophages (BMDMs) (G). (H to M) Relative mRNA expression of Tnf (H), Cxcl9 (I), Cxcl10 (J), Mrc1 (K), Nos2 (L), and Arg1 (M). (N to P) Representative immunoblots of PI3Kγ, total nuclear factor κB (NF-κB) p65, phosphorylated NF-κB p65, and GAPDH (N); quantification of PI3Kγ protein abundance normalized to GAPDH (O); and a heatmap of the phosphorylated-to-total NF-κB p65 ratio (P). (Q to T) Representative immunoblots of inducible nitric oxide synthase (iNOS), CCAAT/enhancer-binding protein β (C/EBPβ), and arginase 1 (Arg1), with β-tubulin as the loading control (Q), and corresponding quantification of C/EBPβ (R), Arg1 (S), and iNOS (T) protein abundance. (U to X) Concentrations of C-X-C motif chemokine ligand 9 (CXCL9; U), CXCL10 (V), tumor necrosis factor-α (TNF-α; W), and interleukin-12 (IL-12; X) in culture supernatants. For panels (D) to (X), G1 represents untreated macrophages, G2 represents INP treatment, G3 represents IMNP treatment, G4 represents INMP treatment, and G5 represents IMNMP treatment. Data were obtained from three independent preparations. Individual measurements and SD are shown where applicable. P values are indicated for the corresponding comparisons.

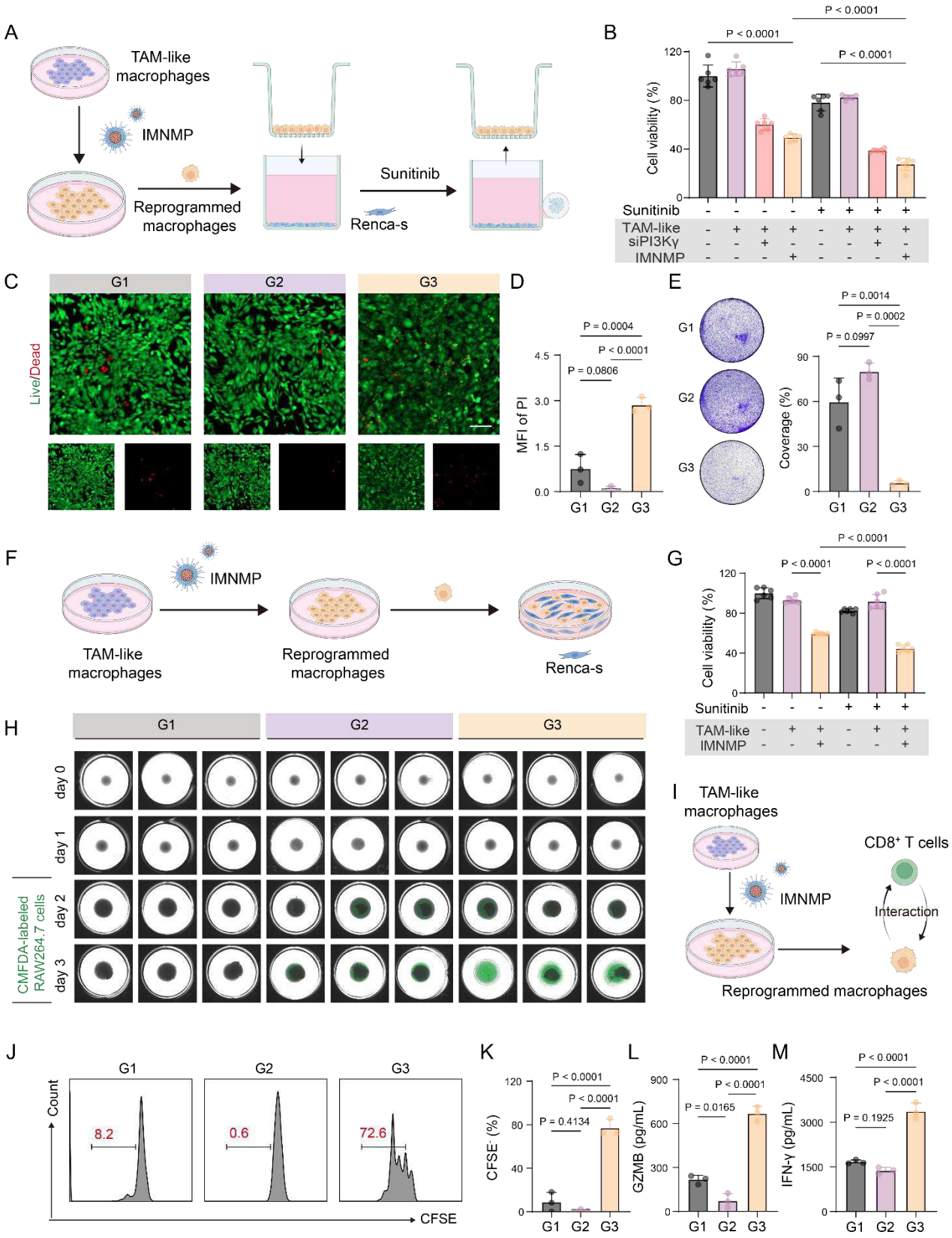


Fig. 5. PI3Kγ-directed macrophage modulation attenuates tumor support and enhances CD8 T-cell responses

(A) Schematic illustration of the noncontact Transwell coculture assay used to evaluate the effects of untreated, Pik3cg siRNA–treated, or IMNMP-pretreated TAM-like macrophages on Renca-s cells. (B) Renca-s cell viability following coculture with the indicated macrophage groups, with or without sunitinib treatment. (C and D) Representative calcein-AM/propidium

iodide (PI) live/dead fluorescence images (C) and quantification of PI mean fluorescence intensity (MFI) (D) in Renca-s cultures under the indicated conditions. (Bar = 100 μm). (E) Representative crystal violet staining and quantification of stained-area coverage following coculture. For panels (C) to (E), G1 represents Renca-s cells cultured alone, G2 represents Renca-s cells cocultured with untreated TAM-like macrophages, and G3 represents Renca-s cells cocultured with IMNMP-pretreated macrophages. Representative wells in (E) are arranged in this order from top to bottom. (F and G) Schematic illustration of the direct-contact macrophage–tumor cell coculture assay (F) and measurement of overall viability in the mixed-cell population, with or without sunitinib treatment (G). (H) Representative images of three-dimensional Renca-s spheroids acquired from day 0 to day 3. G1 represents spheroids cultured alone, G2 represents spheroids cocultured with untreated TAM-like macrophages, and G3 represents spheroids cocultured with IMNMP-pretreated macrophages. Macrophages were labeled with chloromethylfluorescein diacetate (CMFDA). (I) Schematic illustration of the coculture assay involving IMNMP-pretreated TAM-like macrophages and anti-CD3/CD28–stimulated $CD8^+$ T cells. (J and K) Representative carboxyfluorescein succinimidyl ester (CFSE) dilution profiles (J) and quantification of the CFSE-negative $CD8^+$ T-cell fraction (K). GZMB (L) and IFN-γ (M) concentrations in coculture supernatants. For panels (J) to (M), G1 represents activated $CD8^+$ T cells cultured alone, G2 represents activated $CD8^+$ T cells cocultured with untreated TAM-like macrophages, and G3 represents activated $CD8^+$ T cells cocultured with IMNMP-pretreated macrophages. Experiments included three independent preparations, with six technical replicate wells per condition for viability assays. Data are presented as mean ± SD with individual measurements where applicable. P values are indicated for the corresponding comparisons.

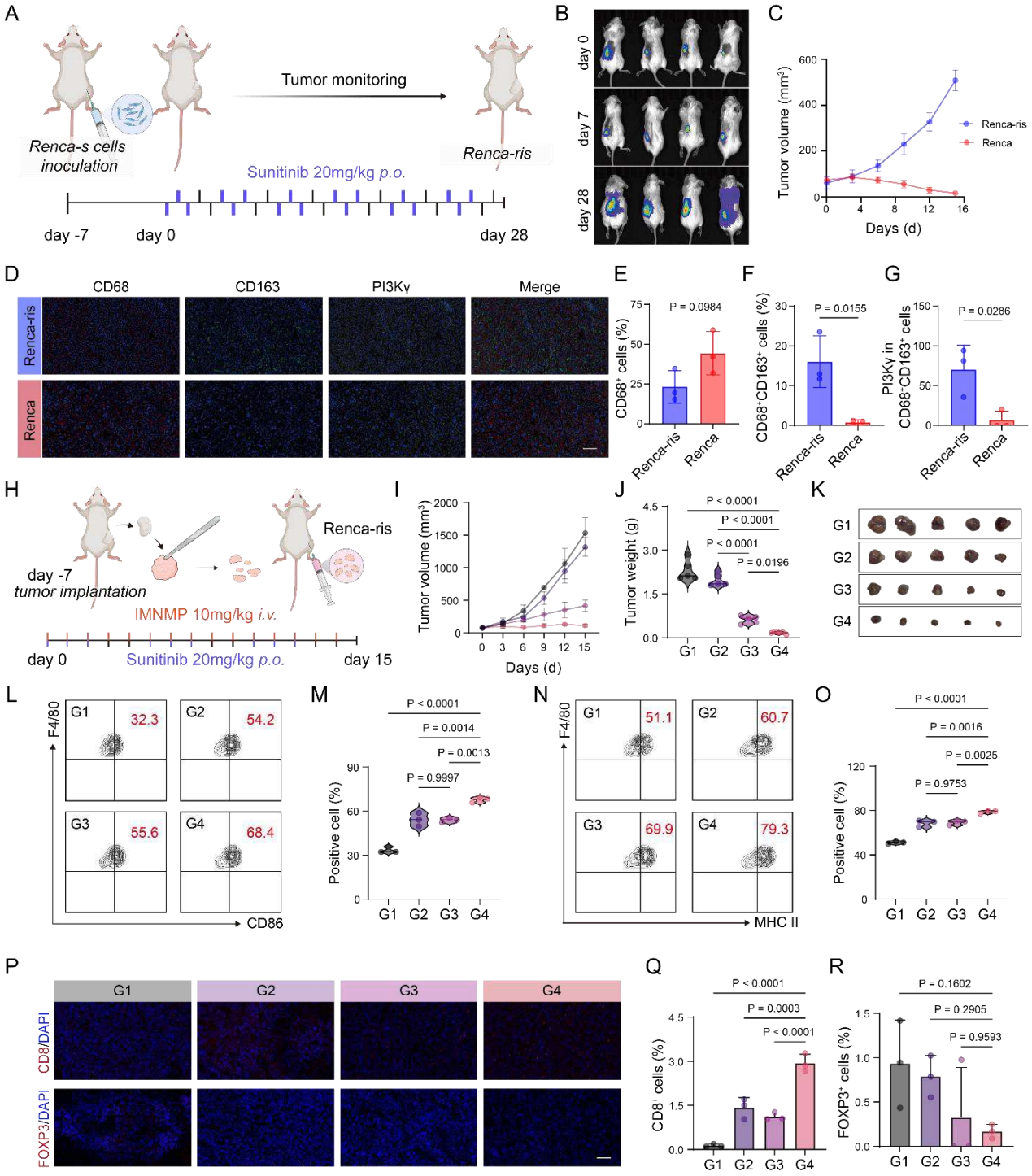


Fig. 6. IMNMP enhances sunitinib-mediated tumor control in treatment-selected subcutaneous renal tumors

(A) Schematic illustration of the establishment of the treatment-selected Renca-ris tumor model through repeated sunitinib administration to mice bearing Renca-s-derived tumors. (B) Representative serial bioluminescence images acquired during Renca-ris model establishment. (C) Tumor growth curves of the indicated Renca-derived groups during subsequent sunitinib treatment. (D) Representative multiplex immunofluorescence images of CD68, CD163, and PI3Kγ in parental Renca and Renca-ris tumor tissues, with nuclear counterstaining (Bar = 100 μm). (E to G) Quantification of $CD68^+$ cell proportions (E), $CD68^+CD163^+$ cell proportions (F), and PI3Kγ positivity within the $CD68^+CD163^+$ population (G). (H) Schematic illustration of the subcutaneous tumor treatment protocol and administration schedule. (I to K) Tumor

growth curves (I), endpoint tumor weights (J), and representative images of excised tumors (K) following the indicated treatments. (L and M) Representative flow cytometry plots of F4/80 and CD86 expression (L) and quantification of $CD86^+$ cells among $F4/80^+$ tumor macrophages (M). (N and O) Representative flow cytometry plots of F4/80 and major histocompatibility complex class II (MHC-II) expression (N) and quantification of $MHC\text{-}II^+$ cells among $F4/80^+$ tumor macrophages (O). (P to R) Representative immunofluorescence images of CD8 and FOXP3 staining in tumor tissues (P), with quantification of $CD8^+$ (Q) and $FOXP3^+$ (R) cell proportions (Bar = 100 μm). For panels (I) to (R), G1 represents untreated controls, G2 represents sunitinib treatment, G3 represents IMNMP treatment, and G4 represents combined sunitinib and IMNMP treatment. Sunitinib was administered orally at 20 mg/kg, and IMNMP was administered intravenously at 10 mg/kg, expressed as the IPI-549-equivalent dose. Efficacy experiments included five mice per group, whereas tissue and immune analyses included three mice per group. Data are presented as mean ± SD with individual measurements where applicable. P values are indicated for the corresponding comparisons.

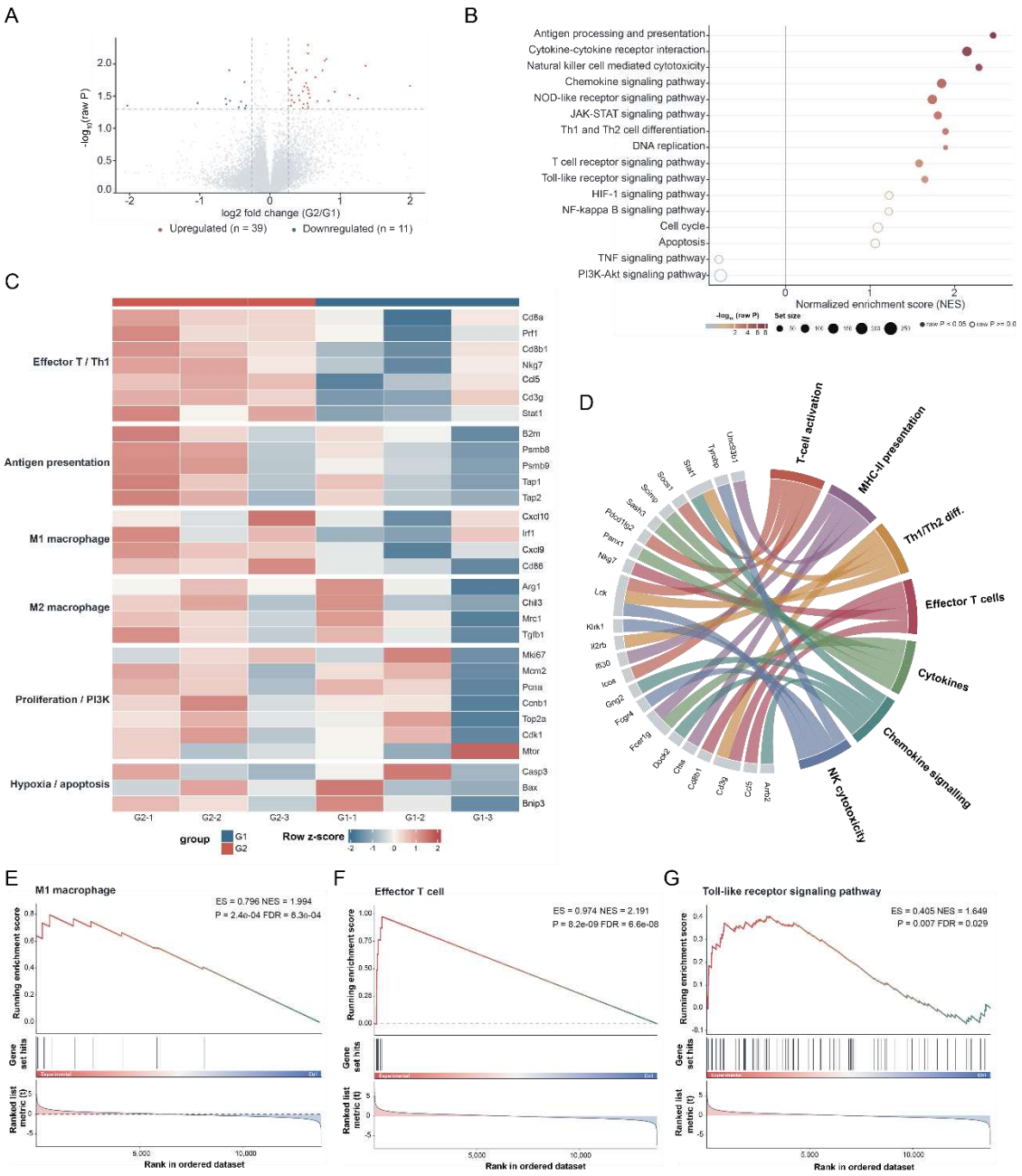


Fig. 7. Bulk tumor transcriptomics reveals antigen-presentation and effector immune signatures associated with sunitinib plus IMNMP treatment

(A) Volcano plot showing $\log_2$ fold changes (G2 versus G1) and $-\log_{10}$ nominal P values. The indicated thresholds identified 39 upregulated and 11 downregulated genes. (B) Pathway enrichment analysis showing normalized enrichment scores (NES) on the horizontal axis. Point size represents gene-set size, and color indicates $-\log_{10}$ nominal P values. Filled and open circles denote nominal $P < 0.05$ and $P \geq 0.05$, respectively. (C) Row-scaled heatmap of selected genes associated with T-cell effector responses, antigen processing and presentation, macrophage-related programs, proliferation, and stress responses. (D) Chord diagram illustrating associations between selected genes and annotated functional modules. (E to G) Gene set enrichment analysis (GSEA) plots for pro-inflammatory macrophage (E; NES = 1.994, false discovery rate (FDR) = 6.3×10^{-4}), effector T-cell (F; NES = 2.191, FDR = 6.6×10^{-8}), and Toll-like receptor signaling (G; NES = 1.649, FDR = 0.029) gene sets. Positive enrichment

indicates enrichment toward the combination-treatment group (G2). G1 represents untreated controls, G2 represents combined sunitinib and IMNMP treatment.

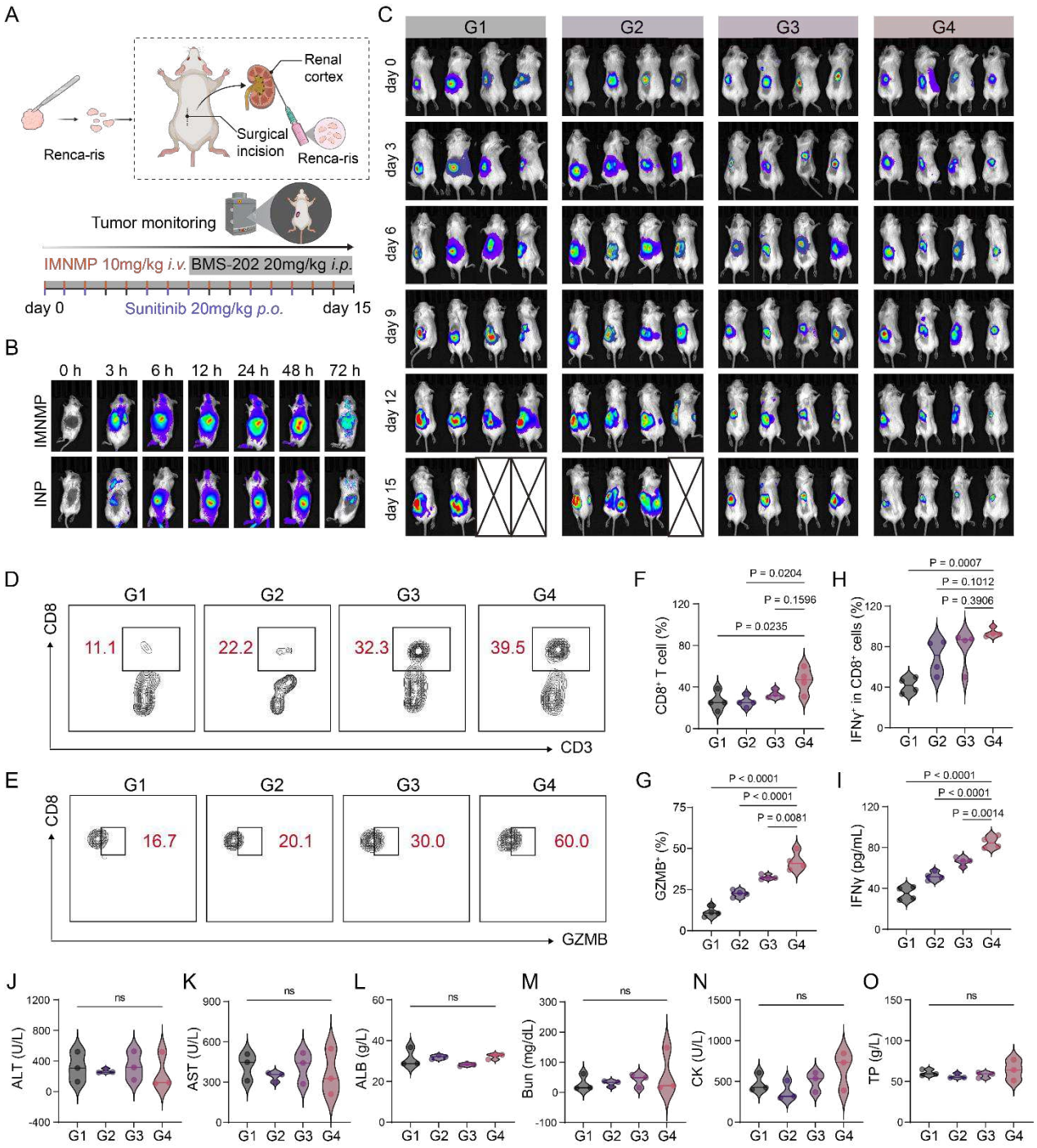


Fig. 8. An IMNMP-containing triplet enhances intratumoral CD8⁺ T-cell effector responses in orthotopic renal tumors

(A) Schematic illustration of Renca-ris tumor implantation into the renal cortex and the treatment schedule. The four treatment groups were G1, sunitinib; G2, sunitinib plus BMS-202; G3, sunitinib plus IMNMP; and G4, sunitinib plus IMNMP and BMS-202. Sunitinib was administered orally at 20 mg/kg, IMNMP intravenously at 10 mg/kg (IPI-549 equivalent), and BMS-202 intraperitoneally at 20 mg/kg. (B) Representative whole-body near-infrared fluorescence images of orthotopic tumor-bearing mice following administration of DiR-labeled IMNMP or INP at matched tracer doses, acquired at 0, 3, 6, 12, 24, 48, and 72 h. (C) Serial bioluminescence images of orthotopic tumors during the 15-day treatment period. Crossed boxes indicate unavailable images. (D and E) Representative flow cytometry plots showing CD3 and CD8 expression (D) and granzyme B (GZMB) expression within the CD8⁺ T-cell

population (E). (F) Quantification of intratumoral $CD3^+CD8^+$ T cells as a proportion of $CD45^+$ leukocytes. (G and H) Quantification of $GZMB^+$ (G) and interferon-γ $(IFN\text{-}\gamma)^+$ (H) cells within the intratumoral $CD3^+CD8^+$ T-cell population. (I) Soluble IFN-γ concentrations in tumor-derived samples. (J to O) Serum biochemical measurements of alanine aminotransferase (ALT; J), aspartate aminotransferase (AST; K), albumin (ALB; L), blood urea nitrogen (BUN; M), creatine kinase (CK; N), and total protein (TP; O). The longitudinal tumor experiment included four mice per group. Immune phenotyping and serum biochemical analyses included three independent mice per group, whereas the separate fluorescence-distribution experiment included five mice per group. Individual measurements are shown where applicable. P values indicate the corresponding comparisons; ns denotes a nonsignificant comparison.

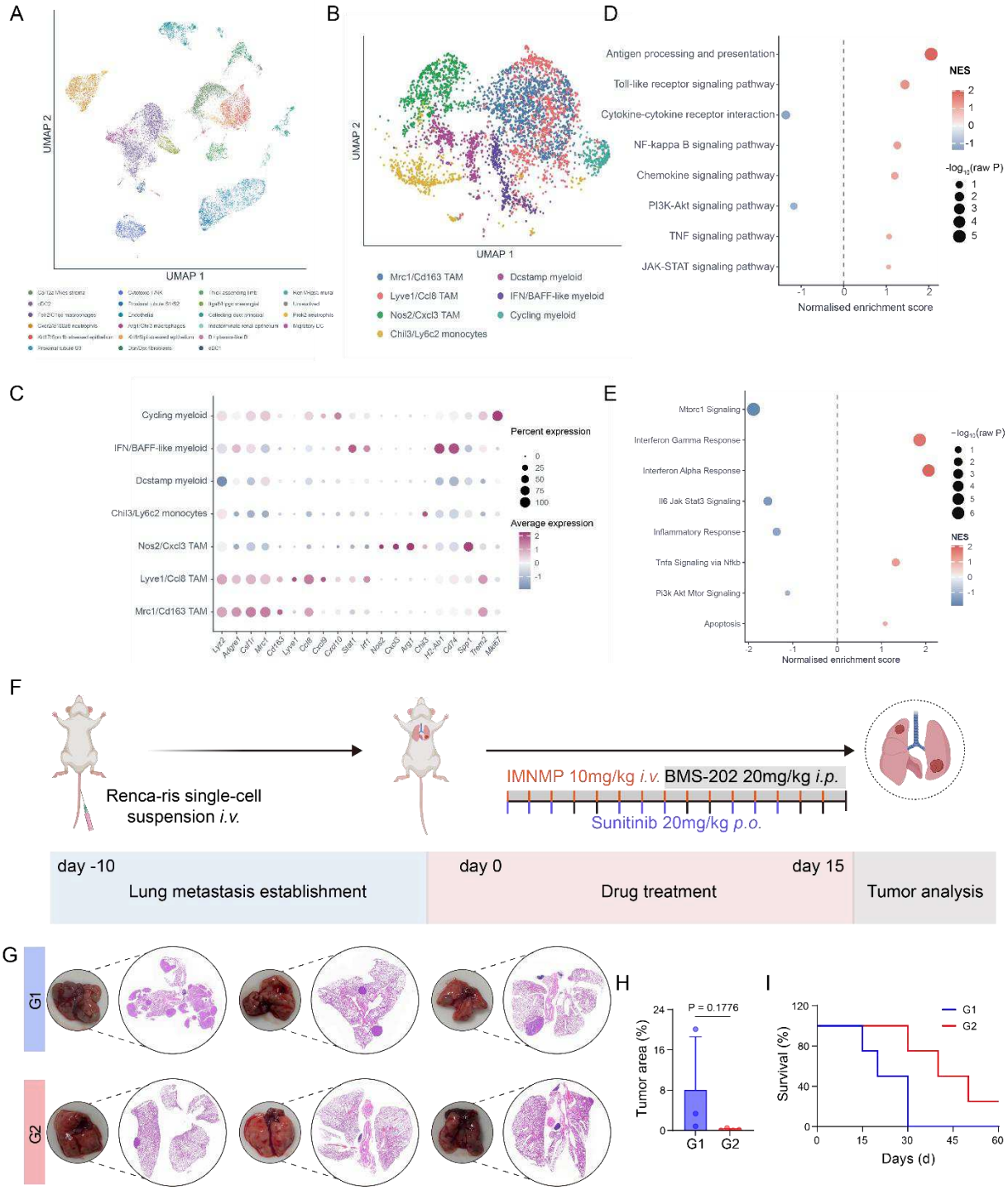


Fig. 9. Triplet-associated myeloid transcriptional signatures in orthotopic renal tumors and treatment outcomes in a pulmonary colonization model

(A) Uniform manifold approximation and projection (UMAP) of 41,693 quality-filtered cells from orthotopic renal tumors treated with sunitinib alone or the triplet regimen, with three independent mice per group. (B) UMAP visualization of the tumor-associated macrophage (TAM)-enriched myeloid compartment (4,115 cells), reclustered into seven transcriptional states. (C) Dot plot showing marker gene expression across the seven myeloid states. Point size represents the proportion of cells expressing each gene, and color indicates average expression. (D and E) Kyoto Encyclopedia of Genes and Genomes (KEGG) pathway enrichment (D) and Hallmark gene set enrichment (E) based on mouse-level pseudobulk comparisons between the

triplet and sunitinib-alone groups. The horizontal axis and point color represent normalized enrichment scores (NES), whereas point size indicates $-\log_{10}$ nominal P values. Positive NES values indicate enrichment in the triplet-treated group. (F) Schematic illustration of the experimental pulmonary colonization model established by intravenous injection of Renca-ris-derived cells, followed by treatment initiation 10 days after inoculation. G1 received sunitinib alone, and G2 received sunitinib plus IMNMP and BMS-202. (G) Representative gross lung images and hematoxylin and eosin (H&E)-stained lung sections from the two treatment groups. (H) Quantification of pulmonary tumor area as a proportion of the analyzed lung tissue area (n = 3 mice per group; P = 0.1776). (I) Kaplan–Meier survival curves from a separate cohort (n = 4 mice per group), with survival monitored from tumor-cell inoculation through day 60.

Supplementary Files

This is a list of supplementary files associated with this preprint. Click to download.

- supplementaryinformation.docx